SIMULTANEOUS LIGHTWAVE INFORMATION AND POWER TRANSFER IN UNDERWATER VISIBLE LIGHT COMMUNICATIONS

A Thesis

by

Sara Ghasvarianjahromi

Submitted to the
Graduate School of Engineering
In Partial Fulfillment of the Requirements for
the Degree of

Master of Science

in the
Department of Electrical and Electronics Engineering

Özyeğin University
July 2021

SIMULTANEOUS LIGHTWAVE INFORMATION AND POWER TRANSFER IN UNDERWATER VISIBLE LIGHT COMMUNICATIONS

Approved by:

Professor Murat Uysal, Advisor
Department of Electrical and Electronics Engineering
Özyeğin University

Assistant Professor Kadir Durak
Department of Electrical and Electronics Engineering
Özyeğin University

Assistant Professor Bahattin Karakaya
Department of Electrical and Electronics Engineering
Istanbul University

Date Approved: 27 July 2021

To my dear family

ABSTRACT

In this thesis, we investigate simultaneous lightwave information and power transfer (SLIPT) for underwater visible light communication systems. We consider four SLIPT methods namely AC-DC separation (ADS), time switching (TS), power splitting (PS) and time switching-power splitting (TS-PS) where the splitting/switching factors are defined as optimization parameters in TS, PS and TS-PS methods. For each of these methods, we derive closed-form expressions for the average harvested energy, bit error rate and spectral efficiency in the presence of underwater turbulence modeled by lognormal statistics. Using these expressions, we determine the optimal splitting factors to maximize the harvested energy while satisfying a given bit error rate value and a given threshold spectral efficiency value. Our results reveal that, if not optimized, SLIPT methods under consideration are outperformed by the simple AC-DC separation (ADS) method which provides the largest harvested energy versus spectral efficiency (HE-SE) region. Optimization of splitting/switching factors extends the HE-SE regions; hence, optimized versions of TS, PS and TS-PS methods are able to significantly outperform ADS for most cases. We further investigate the effect of various channel and system parameters such as water type, turbulence level, beam divergence, receiver aperture size on the harvested energy and quantify the improvements in battery lifetime through the use of SLIPT methods.

ÖZETÇE

Bu tezde, su altı görünür ışık iletişim sistemleri için eşzamanlı ışık dalgası bilgisi ve güç aktarımını (SLIPT) araştırıyoruz. Ayırma/anahtarlama faktörlerinin TS'de optimizasyon parametreleri olarak tanımlandığı AC-DC ayırma (ADS), zaman anahtarlama (TS), güç bölme (PS) ve zaman anahtarlama-güç bölme (TS-PS) olmak üzere dört SLIPT yöntemini ele alıyoruz, PS ve TS-PS yöntemleri. Bu yöntemlerin her biri için, lognormal istatistiklerle modellenen sualtı türbülansı varlığında ortalama hasat edilen enerji, bit hata oranı ve spektral verimlilik için kapalı biçimli ifadeler türetiyoruz. Bu ifadeleri kullanarak, belirli bir bit hata oranı değerini ve belirli bir eşik spektral verimlilik değerini karşılarken, hasat edilen enerjiyi en üst düzeye çıkarmak için en uygun bölme faktörlerini belirleriz. Sonuçlarımız, optimize edilmemişse, söz konusu SLIPT yöntemlerinin, en büyük hasat edilen enerjiye karşı spektral verimlilik (HE-SE) bölgesini sağlayan basit AC-DC ayırma (ADS) yönteminden daha iyi performans gösterdiğini ortaya koymaktadır. Ayırma/anahtarlama faktörlerinin optimizasyonu HE-SE bölgelerini genişletir; bu nedenle, TS, PS ve TS-PS yöntemlerinin optimize edilmiş sürümleri, çoğu durumda ADS'den önemli ölçüde daha iyi performans gösterebilir. Ayrıca su tipi, türbülans seviyesi, ışın sapması, alıcı açıklığı boyutu gibi çeşitli kanal ve sistem parametrelerinin hasat edilen enerji üzerindeki etkisini araştırıyor ve SLIPT yöntemlerini kullanarak pil ömründeki gelişmeleri nicelleştiriyoruz.

Acknowledgements

I would like to express my sincere gratitude to my supervisor, Professor Murat Uysal, for his support, advice, guidance, and encouragement throughout the course of my M.Sc. studies.

I would also like to sincerely thanks the members of my thesis committee, Dr. Kadir Durak and Dr. Bahattin Karakaya for their valuable time and comments on my thesis.

Last, but not least, I would like to express a deep sense of gratitude to my dear parents, Mohammadreza and Parvin and to my one and only loving sister, Parisa whom I owe my life for their endless love, encouragement, support and blessings.

Abbreviations

SLIPT	Simultaneous Lightwave Information and Power Transfer
ADS	AC-DC Separation
TS	Time Switching
PS	Power Splitting
TS-PS	Time Switching-Power Splitting
HE-SE	Harvested Energy-Spectral Efficiency
USNs	Underwater Sensor Networks
AUV	Autonomous Underwater Vehicles
RF	Radio Frequency
VLC	Visible Light Communications
UVLC	Underwater Visible Light Communications
EH	Energy Harvesting
ID	Information Decoding
SWIPT	Simultaneous Wireless Information and Power Transfer
OFDM	Orthogonal Frequency-Division Multiplexing
MIMO	Multiple Input-Multiple Output
DC	Direct Current
AC	Alternating Current
Si	Silicon
PV	Photovoltaics
SISO	Single Input-Single Output
BER	Bit Error Rate

IM/DD	Intensity Modulation and Direct Detection
M-PAM	M-ary pPlse Amplitude Modulation
OOK	On-Off Keying
AWGN	Additive White Gaussian Noise
LN	Lognormal
GG	Gamma-Gamma
PDFs	Probability Density Functions

TABLE OF CONTENTS

LIST OF TABLES

LIST OF FIGURES

CHAPTER I

INTRODUCTION

1.1 Motivation

Advanced sensing, monitoring and surveillance capabilities are required to address the needs of current and emerging maritime applications such as environmental monitoring, port/harbor security, underwater scientific data collection, offshore oil field exploration among others [1]. In an effort to address such demands, there is a growing interest on underwater sensor networks (USNs) and autonomous underwater vehicles (AUVs). While early USNs are typically based on fiber optic, their high installation cost and operational difficulties become restrictive for most cases. With their flexible structure and ease of redeployment, wireless networking provides a powerful alternative. Similarly, AUVs require reliable wireless solutions to communicate with other AUVs, central stations on the shore and sensor nodes [2].

Radio frequency (RF) communications, Acoustic communications and visible light communications can be used as wireless alternatives. In addition to electromagnetic safety and health concerns regarding high-power RF applications, underwater RF communications suffers from high attenuation and low efficiency [3]. RF waves highly attenuate in seawater and can only reach considerable distances at the very low frequency (i.e., 30–300 Hz) in shallow waters which make it impractical for most underwater communication purposes. In addition to that, underwater RF communication requires costly antennas operating with high transmission powers.

Acoustic underwater communications can support transmission ranges in the order of kilometers [4]. They however fall short with their low data rates (in the order of tens of kb/s) for high-bandwidth underwater applications such as real-time image and video transmission. In addition to that, acoustic communications suffers from low available bandwidth and large latencies due to the low propagation speed. It is worth mentioning that acoustic modems are very expensive and consume a high amount of energy.

Compared to RF and acoustic underwater communications, underwater visible light communications (UVLC) through ocean water can cover a broad frequency range and involve transferring a high amount of data in an energy-efficient manner. Therefore, for short and medium ranges (up to several tens of meters), underwater visible light communication (UVLC) has emerged as a high-capacity alternative. Since water is relatively transparent to blue or green light, visible light lasers or LEDs can be used as transmitters for underwater wireless connectivity with data rates up to hundreds of Mb/s. Detailed surveys on UVLC can be found in [5], [6].

A critical system design issue in USNs is the network lifetime which depends on the amount of the available power (i.e., battery capacity) and the power efficiency of sensor nodes. Similarly, energy efficiency is one of the main challenges for long-term autonomy of AUVs. Recharging of the batteries in underwater scenarios is typically very costly and impractical [7]. A promising solution is energy harvesting (EH) where energy can be derived from the environment or other external sources [8]. Simultaneous lightwave information and power transfer (SLIPT) was further proposed in [9], [10] where the received optical signal is used for both EH and information decoding (ID).

1.2 Literature Review

SLIPT, as a complementary technology to UVLC, can provide continuous connectivity and wireless power for devices and sensors in difficult-to-access locations. A significant additional advantage of this technique is the low cost of transmitters and receivers compared to RF and acoustic communication terminals. Several commercially available optical sources and detectors also have small footprints and can easily be integrated into IoUT modules [3].

SLIPT was inspired from the concept of simultaneous wireless information and power transfer (SWIPT) [11] proposed for radio systems. In the implementation of SWIPT, two main methods can be used [12]. In the time switching (TS) method, the receiver switches in time between the modes of EH and ID. The TS method allows for a relatively simple hardware implementation at the receiver, but requires accurate time synchronization and information/energy scheduling. In the other alternative, so-called power splitting (PS) method, the receiver splits the received power into two portions. One portion is used for ID while the other is used for EH in a simultaneous manner [13].

Hybrid versions of TS and PS methods were also proposed [14], [15] where the received signal is split both in the power and time domains. In [14], a hybrid TS-PS method for orthogonal frequency division multiplexing (OFDM) systems was proposed, where the artificial noise is used for both secure information and energy transfer. By optimizing the cyclic prefix length and the power allocation ratio between the information and the noise, the authors maximize the average secrecy rate while doing information decoding (through adopting PS in the second phase of TS), under the constraint on the energy transfer (the first phase of TS). The authors in [15] considered a hybrid TS-PS SWIPT method for a full duplex massive multiple input-multiple output (MIMO) system. The communication is divided into two phases through TS method. In the first phase, the base station transmits energy signals to sensors, and the sensors utilize one portion of the received energy signals for EH and the remaining portion for downlink channel estimation by adopting PS method. In the second phase, the BS forms the transmit beamformers for information transmission to the users and the receive beamformers for receiving signals transmitted by sensors.

AC-DC separation method first proposed as the baseline method to implement SLIPT in VLC system [19], [20]. Since the transmitted optical signal carries a DC component which is not used for data transfer (AC component of the transmitted signal used for data transmission) and can be easily used for energy harvesting purposes, the AC-DC separation method can be implied as the baseline. Using the concept of the ADS method and inspired from SWIPT counterparts, TS, PS and hybrid SLIPT methods were applied to indoor VLC systems, see e.g., [9], [16], [17] to improve the amount of harvested energy.

In VLC systems with SLIPT capability, a main design issue is the choice of receiver. While photodetectors are the common choice for high-speed VLC systems, solar panels can be used as an alternative receiver [9], [18]. The application of SWIPT in the VLC was investigated in [18] using a white LED and silicon (Si) solar cells and the data rate of 3 kbps was reported. The first experimental demonstration of indoor SLIPT was demonstrated in [19] and a data rate of 7 Mb/s was reported using a multi-crystalline silicon solar panel receiver. In [20], the authors experimentally demonstrated the implementation of OFDM for indoor SLIPT using multi-crystalline silicon solar panel receiver and achieved data rate of 11.4 Mb/s with 2 mW harvested power over a link distance of 95 cm. In more recent works, as summarized in Table 1.1, high data rates on the order of hundreds of Mb/s were demonstrated with gallium arsenide [21], [22] and organic solar cells [23], [24].

In [21], the authors experimentally studied SLIPT using a Gallium-arsenide photovoltaic cell for indoor environment. They achieved 0.5 Gbps data rate over a 2 m link and 3.6 mW harvested power. In [22], trade-off between the data rate and harvested energy was experimentally studied for indoor SLIPT system with Gallium-arsenide Photovoltaics (PV) cell at receiver side. A data rate of 784 Mbps with 1 mW harvested power over a link distance of 2 m were achieved. They also achieved the maximum data rate of 1041 Mbps but with a diminished electrical DC power which

Table 1.1: Overview of experimental SLIPT works.

Ref	Environment	Distance	RX Type	Data rate	Harvested energy
[19]	Indoor	39 cm	Multi-crystalline silicon solar panel	7 Mbs	2.1 mW
[20]	Indoor	95 cm	Multi-crystalline silicon solar panel	11.4 Mbps	2 mW
[21]	Indoor	2 m	Gallium-arsenide PV cell	500 Mbps	3.6 mW
[22]	Indoor	2 m	Gallium-arsenide PV cell	784 Mbps	1 mW
[23]	Indoor	1 m	Organic solar cell	34.2 Mbps	0.43 mW
[24]	Indoor	40 cm	Organic solar cell	147.5 Mbps	3.7 mW
[3]	Underwater	30 cm	Monocrystalline silicon solar panel	500 kbps	13.1 mW

was not sufficient for energy harvesting. In [23], an experimental implementation of SLIPT using organic solar cell was demonstrated. The authors reported data rate of 34.2 Mbps and 0.43 mW of harvested power over a 1 m link distance. This paper was particularly important to show that organic solar cells are capable of supporting high speed data communication in the order of tens of Mbps. In [24], the authors experimentally demonstrated the feasibility of simultaneous high-speed data transfer and efficient energy harvesting using a single light source and a single organic solar cell for the single Input-single Output (SISO) setup. The authors reported data rate of 147.5 Mbps and 3.7 mW of harvested power over a 40 cm link distance.

Solar panels are already used for EH purposes in AUVs and USNs [25–28]. This provides a practical motivation for underwater SLIPT to take advantage of the existing infrastructure for both ID and EH. To the best of our knowledge, SLIPT for UVLC was first time explored in [29] where we considered a UVLC system with a semi-collimated laser diode as the transmitter and a solar panel as the receiver and investigated the performance of TS method. In a more recent work [3], experimental demonstration of underwater SLIPT with a multi-crystalline silicon solar panel receiver was successfully carried out where a blue laser was used to charge the battery of a submerged module and some commands were transmitted through 30 cm link. A data rate of 500kbps and harvested power of 13.1 mW were reported. The authors in [3], also discussed the issues related to the hardware and system deployment in harsh environment.

1.3 Thesis Outline

As the literature survey points out, there are very few works on underwater SLIPT. The underwater channels obviously exhibit different propagation characteristics from their indoor counterparts. Not only the path loss model is different, but also underwater channels experience turbulence-induced fading caused by refractive index fluctuations due to salinity and temperature fluctuations. Such differences necessitate a dedicated performance analysis and optimization of SLIPT methods for underwater channels. In an effort to fill this research gap, we develop a framework for UVLC systems with SLIPT capability in this thesis and pursue the performance analysis and optimization of TS and PS methods as well their hybrid versions in underwater channels.

We first present the signal models and SLIPT methods under consideration. Then, we describe the path loss and turbulence-induced fading models to characterize the underwater propagation environment.

Then, taking into account the underwater channel characteristics, we present a comprehensive performance analysis of SLIPT methods for underwater environments. For each SLIPT method under consideration, we derive closed form expressions for the average harvested energy, bit error rate (BER), and spectral efficiency in the presence of underwater turbulence modeled by lognormal statistics. we further define the splitting/switching factors (either in time or power) as an optimization parameter in TS, PS and TS-PS method. We then maximize the amount of harvested energy through the proper selection of splitting/switching factors under the constraints of targeted bit error rate and threshold spectral efficiency.

Finally, we investigate the effect of various channel and system parameters such as water type, turbulence level, beam divergence, receiver aperture size on the harvested energy and quantify the improvements in battery lifetime through the use of SLIPT methods.

1.4 Organization

The rest of this thesis is organized as follows. In chapter 2, we describe the system and channel models and present the SLIPT methods. In chapter 3, we derived closed-form expressions for the harvested energy, BER and spectral efficiency over the lognormal distribution and present the performance analysis and optimization of different SLIPT methods under consideration. In chapter 4, we present numerical results for different water types and investigate the effect of channel and system parameters to corroborate our analytical findings. We finally conclude and summarize thesis in chapter 5.

CHAPTER II

SYSTEM AND CHANNEL MODELS

In this section, we first present the signal models and SLIPT methods under consideration. Then, we describe the path loss and turbulence-induced fading models to characterize the underwater propagation environment.

2.1 UVLC System

As illustrated in Fig. 2.1, we consider a UVLC system with intensity modulation and direct detection (IM/DD). The incoming bit stream is modulated with M-ary pulse amplitude modulation (M-PAM)[1] where M is the modulation size.

Let B_S and τ_d respectively denote the data rate and channel delay spread. A channel is classified as frequency-selective for $B_s\tau_d \geq 1$. If $B_s\tau_d \approx 1$, then it is classified as frequency-flat channel [32]. Underwater optical channels exhibit frequency selectivity only for data rates higher than hundreds of Mb/s. In such cases, multicarrier communication in the form of OFDM is employed to deal with the resulting inter symbol interference. Otherwise, for most underwater practical purposes with moderate data requirements (in the order of tens of Mbps), single-carrier systems with simple modulation techniques such as on-off keying (OOK) and pulse amplitude modulation (PAM) can be used.

We assume a transmission frame with a duration of T_{tot} that consists of N PAM symbols. Without loss of generality, consider a specific signaling interval with a

[1] The delay spread values of underwater optical channels are on the order of a few nanoseconds [30]. Therefore, underwater optical channels exhibit frequency selectivity only for data rates higher than hundreds of Mb/s [31]. Consequently, simple pulse modulation techniques can be employed for most of the underwater applications with moderate data requirements (e.g., in the order of tens of Mb/s).

duration of $T_s = T_{tot}/N$ and let x denote the M-PAM symbol which is represented geometrically as a one-dimensional signal point with possible values of $(m-1)A/(M-1)$ $m = 1, 2..., M$. Here $A \in [0, (I_H - I_L)/2]$ is the peak amplitude where I_L and I_H denote, respectively, the minimum and the maximum input bias current. A DC bias

$$B = I_H - A \tag{2.1}$$

is added to ensure that the resulting signal is non-negative [33]. The instantaneous emitted optical intensity signal can be then written as

$$P_t = S\left(B + x\right) \tag{2.2}$$

where S is the slope efficiency of laser diode.

The transmitted optical signal goes through the underwater propagation medium and is subject to both path loss and turbulence-induced fading. The instantaneous received optical power can be expressed as $P_r = IhP_t$ where I and h respectively denote the fading and path loss terms (see Section 2.3). Under the assumption of quasi-static fading, I remains constant over a block of symbols. The solar panel converts the optical intensity into an electrical current. The received electrical signal is given by [9]

$$i_r = \underbrace{rIhSB}_{I'_{DC}} + \underbrace{rIhSx}_{I_{AC}} + n \tag{2.3}$$

where I'_{DC} and I_{AC} denote the DC and AC components. Here, r is the solar panel responsivity and n is the additive white Gaussian noise (AWGN) with zero mean and variance of σ^2.

2.2 SLIPT Methods

The way of processing the received signal for EH and ID purposes depends on the employed SLIPT method. Let $T_{EH} \leq T_{tot}$ and $T_{ID} \leq T_{tot}$ respectively denote the time durations assigned to EH and ID modes. Furthermore, let us define

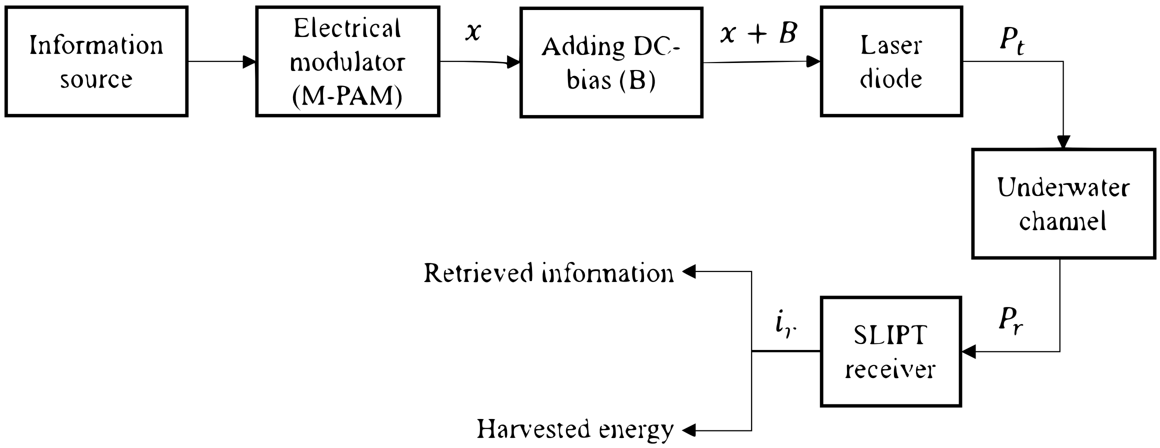

Figure 2.1: System model.

$I_{DC} = I'_{DC} + \iota\zeta\overline{I}_{AC}$[2] where ζ is the AC-to-DC conversion efficiency[3] [16] and ι is an indicator variable (that takes the value of either 0 or 1) to indicate whether or not AC component is used for EH. If only DC component is used for EH, then ι is set as zero. Here, $\overline{I}_{AC} = rIhSE[x]$ denotes the average of AC component where $SE\left[x\right] = (S/M)\sum_{m=1}^{M}\left(\left(m-1\right)A\right)/(M-1) = SA/2$ is the average optical transmit power. In our work, we consider four different SLIPT methods as detailed below.

AC-DC Separation (ADS) method: In this simple method [19], [20], which will be used to benchmark more complicated SLIPT methods, AC and DC components of the received signal are separated in a straightforward manner and, respectively, used for ID and EH purposes (see Fig. 2.2). Since ID and EH blocks are simultaneously active, we have $T_{ID} = T_{EH} = T_{tot}$. We assume that A takes the maximum value, i.e., $A = (I_H - I_L)/2$. Therefore, B is set as the mid-point of linear region of laser diode, i.e., $B = (I_L + I_H)/2$. The AC component of the received signal is blocked by an inductor, i.e., $\iota = 0$, and I'_{DC} is fed to EH block. The DC component of the received signal is blocked by a capacitor and $\overline{I}_{AC} + n$ is fed to ID block to retrieve the message.

[2]Effect of noise is negligible in DC component of received signal and hence ignored [16].
[3]To harvest energy from AC component, an AC/DC converter can be employed. For this purpose, rectifiers are used in practice [34], [35]. Conversion efficiency of a rectifier is defined as the ratio of DC output power to the input power from the AC supply.

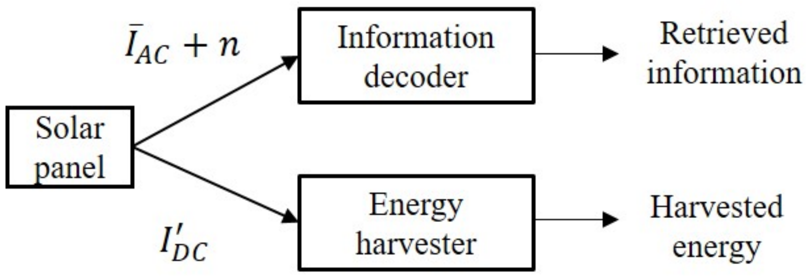

Figure 2.2: Receiver architecture for ADS

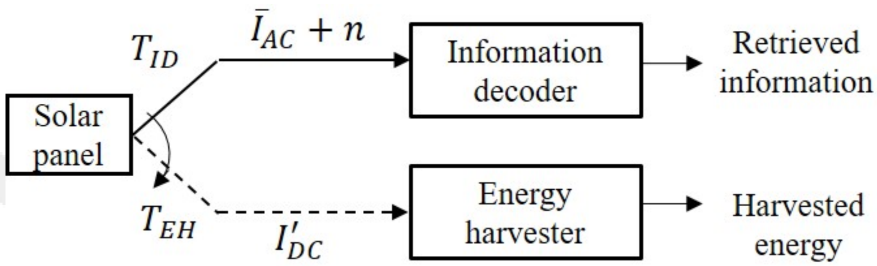

Figure 2.3: Receiver architecture for TS

TS method: In TS method (Fig. 2.3), the receiver switches in time between the modes of EH and ID. Let τ $(0 \leq \tau \leq 1)$ denotes the time switching factor. Therefore, $T_{EH} = (1-\tau) T_{tot}$ and $T_{ID} = \tau T_{tot}$ are respectively dedicated for EH and ID modes [12]. When the receiver operates in EH mode, the DC bias is set to take its maximum value given by $B = I_H$ to maximize harvested energy. This effectively leads to $A = 0$ in (2.1), i.e., x carries no information. The resulting DC signal is fed to EH block. When the receiver operates in ID mode, the DC component is blocked and the rest of the signal, i.e., $\overline{I}_{AC} + n$, is used for demodulation.

PS method: In PS method (Fig. 2.4), we have simultaneous ID and EH during the whole transmission block, i.e., $T_{ID} = T_{EH} = T_{tot}$. The received signal power is split into two streams with a factor of $0 \leq \rho \leq 1$. Therefore, $(1-\rho) i_r$ and ρi_r are respectively dedicated for EH and ID modes. With the proper suppression of AC or DC components, the inputs of EH and ID blocks take the form of $(1-\rho)\left(I'_{DC} + \zeta \overline{I}_{AC}\right)$ and $\rho\left(\overline{I}_{AC} + n\right)$, respectively.

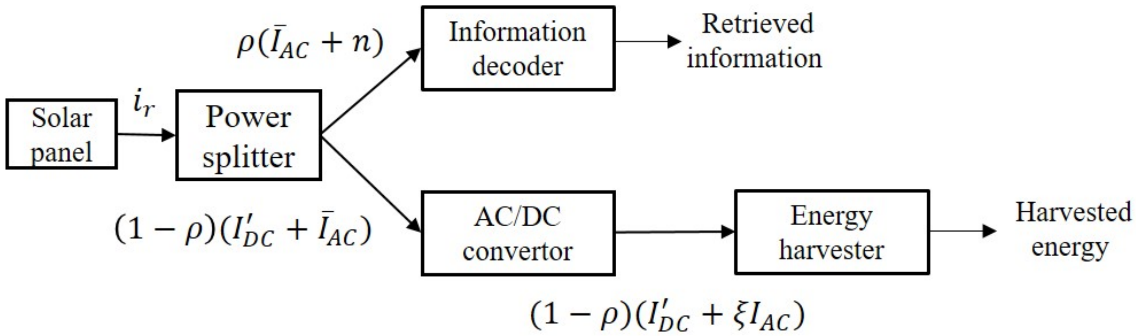

Figure 2.4: Receiver architecture for PS

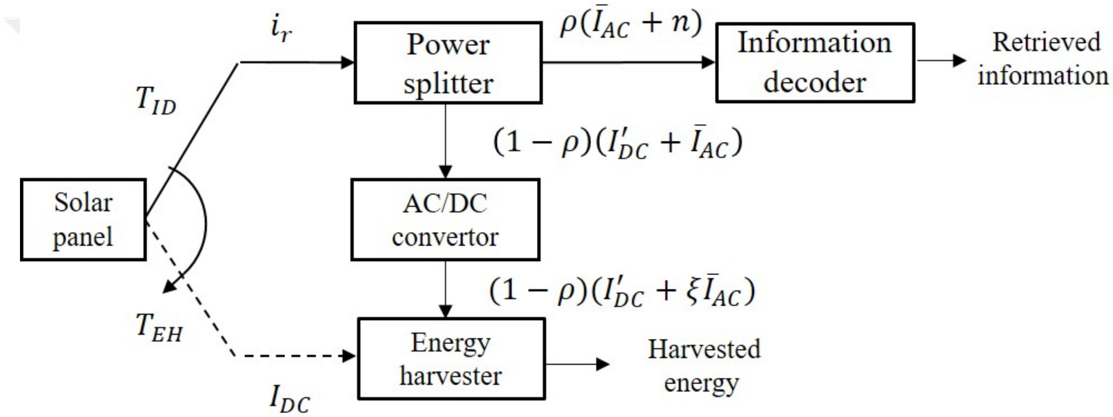

Figure 2.5: Receiver architecture for TS-PS

Hybrid TS-PS method: This method (Fig. 2.5) is basically the combination of TS and PS methods. Since the signal carries both AC and DC components in the ID mode of TS method, it is possible to apply the PS method to take advantage of the existing DC component for EH purpose as well during this period. Building upon this motivation, the hybrid SLIPT method has two phases. In the first phase with a duration of $T_{ID} = \tau T_{tot}$, the receiver adopts PS method to perform EH and ID simultaneously. The received signal power is split into two streams with a splitting factor of ρ. The resulting streams, i.e., $(1-\rho)\left(I'_{DC} + \zeta \overline{I}_{AC}\right)$ and $\rho\left(\overline{I}_{AC} + n\right)$, are respectively fed to EH and ID blocks. In the second phase with a duration of $T_{EH} = (1-\tau)\, T_{tot}$, only EH mode is active (similar to TS method). In this phase, the transmitted signal carries no information and therefore DC bias can be set to its maximum value ($B = I_H$) to maximize the harvested energy.

2.3 Channel Model

The path loss is found as the summation of attenuation loss and geometrical loss. The latter occurs due to the spreading of the transmitted beam between the transmitter and the receiver. The attenuation loss is determined by absorption and scattering. To calculate underwater attenuation loss, the Beer-Lambert (BL) formula [36] is commonly used in the literature. BL formula however builds upon the implicit assumptions that the transmitter and receiver are perfectly aligned and all the scattered photons are lost and therefore results in the overestimation of the path loss. Even though in reality some of the scattered photons can still arrive at the receiver after multiple scattering events. According to the BL, path loss can be shown as

$$h_{BL} = \exp\left(-cd\right) \tag{2.4}$$

where d is the link distance, c is the extinction coefficient. The overall path loss contains both attenuation loss and geometrical loss and can be obtained as the summation of these terms as

$$h \approx \left(\frac{D_R}{\theta_F}\right)^2 d^{-2} \exp\left(-cd\right) \tag{2.5}$$

Building upon a modified version of the BL formula to take into account the contribution of scattered rays, an underwater path loss formula was presented in [31]. According to this formula, the path loss term is given by

$$h \approx \left(\frac{D_R}{\theta_F}\right)^2 d^{-2} \exp\left(-c\left(\frac{D_R}{\theta_F}\right)^{\vartheta} d^{1-\vartheta}\right) \tag{2.6}$$

where ϑ is a correction coefficient based on water type [31], θ_F is the full width transmitter beam divergence angle and D_R is the receiver aperture diameter.

Another impairment is underwater turbulence caused by refractive index fluctuations due to salinity and temperature fluctuations and presence of air bubbles in seawater. These factors can lead to rapid changes in the refractive index of the water and affect the intensity of turbulence [37], [38], [39]. For example, salinity fluctuations caused by storm precipitation and terrestrial freshwater runoff can be an effective factor which results in excess drop in salinity and, therefore, a significant increase in scintillation index [38]. Air bubbles, as an another influential factor, are very strong scatters and can result in heavy attenuation that affect propagation of optical signals [39]. The effect of air bubbles on turbulence strength is more pronounced at depths near to the sea surface due to the effect of surface tension [40] and in saline water [41]. In general, we can say that turbulence effect becomes stronger as the horizontal propagation comes close to the surface of the water, whereas the turbulence effect is quite small in the deep water boundary [42].

This turbulence causes the received signal intensity to fluctuate over its average also known as fading. Lognormal (LN) and Gamma-Gamma (GG) probability density functions (PDFs) were shown to match the measurement results [43–45] respectively for weak[4] and moderate/strong turbulence.

Under the assumption of weak turbulence which is *typically* observed for short link distances [5][37], the fading coefficient I is modelled with LN distribution. Its PDF is given by

$$f_I\left(I\right) = \frac{1}{I\sqrt{2\pi\ \left(4\sigma_x^2\right)}} \exp\left(-\frac{\left(\ln\left(I\right) - 2\mu_x\right)^2}{2\left(4\sigma_x^2\right)}\right) \tag{2.7}$$

where μ_x and σ_x respectively denote the mean and variance of the log-amplitude coefficient $X = 0.5\ln\left(I\right)$. To ensure that the fading coefficient does not change the value of average power, the fading amplitude is normalized such that $E\left[I\right] = 1$, which implies $\mu_x = -\sigma_x^2$ [43]. The relation between log-amplitude variance and the scintillation index is given by $\sigma_x^2 = 0.25\ln\left(1 + \sigma_I^2\right)$. Under the assumption of spherical

[4]The strength of optical turbulence is typically quantified by scintillation index. Scintillation index values $\sigma_I^2 < 1$ are deemed to be weak turbulence [43].

[5]Based on the existence of air bubbles, salinity variations or water depth, strong oceanic turbulence may occur in some cases [40], [42], but weak turbulence is more common for short link distances.

waves, the scintillation index is calculated as [46]

$$\sigma_I^2 = 8\pi^2 k_0^2 d \int_0^1 \int_0^\infty \kappa \, \Phi_n(\kappa) \left\{ 1 - \cos\left[\frac{d\kappa^2}{k_0} \zeta (1-\zeta) \right] \right\} d_\kappa d_\zeta \tag{2.8}$$

where λ is wavelength and $k_0 = 2\pi/\lambda$ is the wave number. In (2.8), $\Phi_n(\kappa)$ is the spatial power spectrum model of turbulent fluctuations of the sea-water refraction index. It depends on temperature and salinity profiles and its calculation can be found in [46]. For the convenience of the reader, this calculation is summarized in the Appendix A.

CHAPTER III

PERFORMANCE ANALYSIS AND OPTIMIZATION

As performance metrics, we consider harvested energy, BER and spectral efficiency. In the following, we first define these three metrics conditioned on the turbulence-induced fading coefficient. Then, we take expectation with respect to LN distribution and find closed-form expressions for each of them. Finally, we use these derived expressions to optimize the SLIPT methods under consideration. Specifically, we determine the optimum value of time and/or power splitting factors to maximize the amount of harvested energy while satisfying the constraints on BER and spectral efficiency.

3.1 Performance Metrics

Harvested Energy: The ideal output power of solar panel in EH mode is given by $P = I_{DC}V_{OC}$ [47] where V_{oc} is the open circuit voltage and calculated as [48] $V_{OC} = V_t \ln(1 + I_{DC}/I_0)$. Here V_t is the thermal voltage and I_0 is the dark saturation current. For the best performance, a solar panel must operate at its maximum power point (MPP) [35]. Dynamic tracking techniques [49] can be used to automatically find the optimal values of MPP voltage (V_{MPP}) and MPP current (I_{MPP}) for a given temperature and irradiance. The maximum output power of solar panel is then given by [49] $P_{MPP} = FI_{DC}V_{OC}$ where $F = I_{MPP}V_{MPP}/I_{DC}V_{OC}$ is the fill factor. Multiplying T_{EH} with P_{MPP} and replacing the definition of V_{OC} therein, the harvested energy (conditioned on I) can be written as [47]

$$E = T_{EH}FI_{DC}V_t \ln\left(1 + \frac{I_{DC}}{I_0}\right) \tag{3.1}$$

BER: Conditioned on the fading coefficient, I, BER of M-PAM is given by (see Appendix B) [50], [51]

$$BER \approx \frac{T_{ID}}{T_{tot}} \frac{2\left(M-1\right)}{M \log_2 M} Q\left(\sqrt{\frac{\gamma}{2(M-1)^2}}\right) \tag{3.2}$$

where γ denotes the average electrical signal-to-noise ratio (SNR). Based on the AC component which carries the message, γ can be written as [52], [53]

$$\gamma = \frac{\left(rIhSE\left[x\right]\right)^2}{\sigma^2} \tag{3.3}$$

where $\sigma^2 = N_0/2T_s$ is the noise variance, and N_0 is the noise power spectral density.

Spectral Efficiency: Conditioned on the fading coefficient I, a lower bound of the spectral efficiency (in b/s/Hz) for IM/DD systems is given by [54]

$$\eta \geq \frac{T_{ID}}{T_{tot}} \left[\frac{1}{2} \log_2 \left(1 + \frac{e}{2\pi}\gamma\right)\right] \tag{3.4}$$

3.2 AC-DC Separation (ADS)

Setting $T_{EH} = T_{tot}$ and $\iota = 0$ in (3.1), the harvested energy for ADS method is obtained as

$$E_{ADS} = T_{tot} F I'_{DC} V_t \ln\left(1 + \frac{I'_{DC}}{I_0}\right) \tag{3.5}$$

Averaging over the PDF in (2.7), the average harvested energy can be expressed as

$$\begin{aligned} \overline{E}_{ADS} = & \int_0^\infty T_{tot} F rIhSB V_t \ln\left(1 + \frac{rIhSB}{I_0}\right) \\ & \times \frac{1}{I\sqrt{2\pi\left(4\sigma_x^2\right)}} \exp\left(-\frac{\left(\ln\left(I\right) - 2\mu_x\right)^2}{2\left(4\sigma_x^2\right)}\right) dI \end{aligned} \tag{3.6}$$

The integral in (3.6) unfortunately does not directly yield a closed-form solution. In an effort to solve it, we use the Holtzman approximation which is an improved version of Gaussian approximation with high accuracy proposed in [55]. Let φ denote a function of normally distributed variable z with mean μ_z and variance σ_z^2. The expectation of $\varphi(z)$ can be approximated as [55]

$$E[\varphi(z)] \approx \frac{2}{3}\varphi(\mu_z) + \frac{1}{6}\varphi\left(\mu_z + \sqrt{3}\sigma_z\right) + \frac{1}{6}\varphi\left(\mu_z - \sqrt{3}\sigma_z\right) \tag{3.7}$$

In our case, we first define $\varphi(z) = \exp(z)\ln(1 + r\exp(z)\, hS\,(I_L + I_H)/2I_0)$ where $z = \ln(I)$. Based on the statistical model described in Section 2.3, it can be readily confirmed that z has a mean of $2\mu_x$ and variance of $4\sigma_x^2$. Rewriting (3.6) as a function of z and using (3.7), we obtain the average harvested energy as (3.8)

$$\begin{aligned} \overline{E}_{ADS} &= T_{tot}FrhSBV_t \int_0^\infty \varphi(z) \frac{1}{\sqrt{2\pi\ (4\sigma_x^2)}} \exp\left(-\frac{(z - 2\mu_x)^2}{2(4\sigma_x^2)}\right) dz \\ &\approx \frac{1}{2} T_{tot} FrhS(I_L + I_H) V_t \\ &\times \left[\frac{2}{3}\varphi(2\mu_x) + \frac{1}{6}\varphi\left(2\mu_x + \sqrt{3}(2\sigma_x)\right) + \frac{1}{6}\varphi\left(2\mu_x - \sqrt{3}(2\sigma_x)\right)\right] \end{aligned} \tag{3.8}$$

For BER calculation, we set $T_{ID} = T_{tot}$ in (3.2) and average the resulting expression with respect to I by using Holtzman approximation. This yields (3.9)

$$\begin{aligned} \overline{BER}_{ADS} &= \int_0^\infty \frac{2(M-1)}{M\log_2 M} Q\left(\sqrt{\frac{(rIhSA)^2}{4\sigma^2(M-1)^2}}\right) \frac{1}{I\sqrt{2\pi\ (4\sigma_x^2)}} \exp\left(-\frac{(\ln(I) - 2\mu_x)^2}{2(4\sigma_x^2)}\right) dI \\ &\approx \frac{2(M-1)}{M\log_2 M}\left[\frac{2}{3}Q\left(\frac{rhSAe^{2\mu_x}}{M-1}\sqrt{\frac{T_s}{N_0}}\right) + \frac{1}{6}Q\left(\frac{rhSAe^{2\mu_x+2\sqrt{3}\sigma_x}}{M-1}\sqrt{\frac{T_s}{N_0}}\right)\right. \\ &\left. + \frac{1}{6}Q\left(\frac{rhSAe^{2\mu_x-2\sqrt{3}\sigma_x}}{M-1}\sqrt{\frac{T_s}{N_0}}\right)\right] \end{aligned} \tag{3.9}$$

Similarly, expectation of (3.4) with respect to I yields the average spectral efficiency in (3.10) as

$$\begin{aligned}\overline{\eta}_{ADS} =& \int_{0}^{\infty} \left[\frac{1}{2}\log_2\left(1+\frac{e(rIhSA)^2 T_s}{4\pi N_0}\right)\right] \frac{1}{I\sqrt{2\pi\ (4\sigma_x^2)}} \exp\left(-\frac{(\ln(I)-2\mu_x)^2}{2\,(4\sigma_x^2)}\right) dI \\ \approx& \frac{1}{2}\left[\frac{2}{3}\log_2\left(1+\frac{e(rhSAe^{2\mu_x})^2 T_s}{4\pi N_0}\right) + \frac{1}{6}\log_2\left(1+\frac{e\left(rhSAe^{2\mu_x+2\sqrt{3}\sigma_x}\right)^2 T_s}{4\pi N_0}\right)\right. \\ &\left. + \frac{1}{6}\log_2\left(1+\frac{e\left(rhSAe^{2\mu_x-2\sqrt{3}\sigma_x}\right)^2 T_s}{4\pi N_0}\right)\right]\end{aligned} \tag{3.10}$$

3.3 Time-Switching (TS)

The average harvested energy for TS method will have the same form of (3.8) where T_{tot} and B are simply replaced by $(1-\tau)\,T_{tot}$ and I_H. This yields

$$\begin{aligned}\bar{E}_{TS} \approx& (1-\tau)\,T_{tot} FrhSI_H V_t\,\left[\frac{2}{3}\varphi\,(2\mu_x)\right. \\ &\left. +\frac{1}{6}\varphi\left(2\mu_x+\sqrt{3}\,(2\sigma_x)\right)+\frac{1}{6}\varphi\left(2\mu_x-\sqrt{3}\,(2\sigma_x)\right)\right]\end{aligned} \tag{3.11}$$

The average BER for TS method $\overline{BER}_{TS}$ will have the same form of (3.9), however it should be taken into account the fact that the receiver works in ID mode for a duration of $T_{ID}=\tau T_{tot}$ i.e., τN symbols out of N symbols. Therefore, we can write

$$\overline{BER}_{TS} = \tau\overline{BER}_{ADS} \tag{3.12}$$

Similarly, average spectral efficiency for TS method can be obtained by multiplying $\overline{\eta}_{ADS}$ in (3.10) by τ. Therefore, we have

$$\overline{\eta}_{TS} = \tau\overline{\eta}_{ADS} \tag{3.13}$$

In the following, we aim to maximize the average harvested energy by proper choice of τ while satisfying given values of targeted BER and spectral efficiency. Let BER_t

and η_{th} respectively denote the required maximum BER value and the minimum spectral efficiency. Mathematically speaking, we can write our optimization problem as

$$
\begin{aligned}
&\max_{\tau} \bar{E}_{TS}(\tau) \\
&s.t. \quad C_1 : \ \overline{BER}_{TS} \leq BER_t \\
&\qquad C_2 \ : \overline{\eta}_{TS} \geq \eta_{th} \\
&\qquad C_3 : \ 0 \leq \tau \leq 1
\end{aligned}
\tag{3.14}
$$

Replacing (3.12) in the first constraint, C_1 can be written as an upper bound on τ, i.e., $\tau \leq BER_t \big/ \overline{BER}_{ADS}$. Based on the relationship between $\overline{\eta}_{TS}$ and $\overline{\eta}_{ADS}$ in (3.13), the second constraint C_2 can be written as a lower bound on τ, i.e., $\tau \geq \eta_{th}/\overline{\eta}_{ADS}$. Further noting the range of τ in the third constraint C_3 (i.e., $0 \leq \tau \leq 1$), we can combine three constraints into a single constraint and rewrite the optimization problem as

$$
\begin{aligned}
&\max_{\tau} \bar{E}_{TS}(\tau) \\
&s.t.\, C_4 : \max\left(0, \frac{\eta_{th}}{\overline{\eta}_{ADS}}\right) \leq \tau \leq \min\left(\frac{BER_t}{\overline{BER}_{ADS}}, 1\right)
\end{aligned}
\tag{3.15}
$$

It can be readily checked from (3.11) that $\bar{E}_{TS}$ is proportional to $1-\tau$. Therefore, to maximize the average harvested energy, we need to choose the minimum value of τ while satisfying the constraint C_4 in (3.15). The minimum value of τ in C_4 therefore becomes the optimal value and is given by

$$
\tau_{opt} = \frac{\eta_{th}}{\overline{\eta}_{ADS}} \tag{3.16}
$$

3.4 Power Splitting (PS)

The average BER for PS method $\overline{BER}_{PS}$ can be obtained from (3.9) where $\overline{I}_{AC}$ should be multiplied by the splitting factor ρ. Similarly, average spectral efficiency $\overline{\eta}_{PS}$ can be obtained from (3.10).

To calculate the average harvested energy for PS method, we first set $T_{EH} = T_{tot}$, $\iota = 1$ in (3.1) and also replace I_{DC} with $(1-\rho)\, I_{DC}$ to take into account power splitting. Following the same steps for derivation of (3.8), we obtain

$$\begin{aligned}\overline{E}_{PS}(\rho) \approx\, & T_{tot}F(1-\rho)\, rhS(B+\zeta A/2)\, V_t \\ & \times\left[\frac{2}{3}\psi(2\mu_x)+\frac{1}{6}\psi\left(2\mu_x+\sqrt{3}(2\sigma_x)\right)+\frac{1}{6}\psi\left(2\mu_x-\sqrt{3}(2\sigma_x)\right)\right]\end{aligned} \tag{3.17}$$

where $\psi(z)=\exp(z)\ln(1+(1-\rho)\, r\exp(z)hS(B+\zeta A/2)/I_0)$.

To maximize the average harvested energy by proper choice of ρ, we can write the optimization problem as

$$\begin{aligned}&\max_{\rho}\, \bar{E}_{PS}(\rho)\\ &s.t.\quad C_5:\ \overline{BER}_{PS}\le BER_t\\ &\qquad\ \ C_6\ :\overline{\eta}_{PS}\ge \eta_{th}\\ &\qquad\ \ C_7:\ 0\le\rho\le 1\end{aligned} \tag{3.18}$$

First we work on the solution of the first constraint C_5. Based on the form of (3.9), it can be noted that $\overline{BER}_{PS}$ is a summation of three Q-function terms. This cannot be solved for ρ in the current form. For sufficiently high SNR (i.e., $\gamma \gg 1$), the third term with smaller argument will be dominant because Q(.) is a decreasing function. Therefore, we can approximate $\overline{BER}_{PS}$ based on Gaussian Q-function approximation as

$$\overline{BER}_{PS} \approx \frac{M-1}{3M\log_2 M}Q\left(\frac{rh\rho_1 SAe^{2\mu_x-2\sqrt{3}\sigma_x}}{2(M-1)}\sqrt{\frac{T_s}{N_0}}\right) \tag{3.19}$$

Solving (3.19) for ρ and then replacing the resulting solution within the constraint C_5, we have

$$\rho\ge\underbrace{\left(Q^{-1}\left(\frac{3BER_t M\log_2 M}{M-1}\right)\left(\frac{2(M-1)}{rhSAe^{2\mu_x-2\sqrt{3}\sigma_x}}\sqrt{\frac{N_0}{T_s}}\right)\right)}_{\rho_1} \tag{3.20}$$

Then, we work on the solution of the second constraint C_6. Considering that SNR is sufficiently high, we can approximate $\overline{\eta}_{PS}$ as

$$\overline{\eta}_{PS} \approx \frac{1}{2}\left[\frac{2}{3}\log_2\left(\frac{e(\rho_2 rhSAe^{2\mu_x})^2 T_s}{4\pi N_0}\right) + \frac{1}{6}\log_2\left(\frac{e\left(\rho_2 rhSAe^{2\mu_x+2\sqrt{3}\sigma_x}\right)^2 T_s}{4\pi N_0}\right)\right.$$
$$\left. + \frac{1}{6}\log_2\left(\frac{e\left(\rho_2 rhSAe^{2\mu_x-2\sqrt{3}\sigma_x}\right)^2 T_s}{4\pi N_0}\right)\right] \tag{3.21}$$

We raise both sides of (3.21) by power two to eliminate the log term and solve it for ρ as

$$\rho_2^{12} \approx \left(\frac{4\pi N_0}{eT_s(rhSA)^2}\right)^6 \frac{2^{12\overline{\eta}_{PS}}}{\left(e^{2\mu_x}\right)^8\left(e^{2\mu_x+2\sqrt{3}\sigma_x}\right)^2\left(e^{2\mu_x-2\sqrt{3}\sigma_x}\right)^2} \tag{3.22}$$

Replacing the resulting solution of (3.22) within the constraint C_6, we can obtain the lower bound of ρ as

$$\rho \geq \underbrace{\frac{2^{\overline{\eta}_{th}} e^{-2\mu_x-\frac{1}{2}}}{rhSA}\sqrt{\frac{4\pi N_0}{T_s}}}_{\rho_2} \tag{3.23}$$

Noting the range of splitting factor ρ in the third constraint C_7, we can combine three constraints into a single constraint, Then we can rewrite the optimization problem in (3.18) as

$$\begin{aligned} &\max_{\tau} \bar{E}_{PS}(\rho) \\ &s.t. \quad C_8 : \max(0, \rho_1, \rho_2) \leq \rho \leq 1 \end{aligned} \tag{3.24}$$

From (3.17), it is observed that $\overline{E}_{PS}$ is dependent on $1-\rho$. Therefore, to maximize the average harvested energy, we need to choose the minimum value of ρ while satisfying the constraint C_8. From the form of C_8, it is straightforward to conclude that the optimal value of ρ is

$$\rho_{opt} = \max(\rho_1, \rho_2) \tag{3.25}$$

3.5 Time Switching and Power Splitting (TS-PS)

The average harvested energy in Time Switching and Power Splitting (TS-PS) method contains two terms resulting from the first and second phases. To calculate the first term, we first set $\iota = 1$, $T_{EH} = \tau T_{tot}$ in (3.1) and multiply I_{DC} with $1 - \rho$. To calculate the second term, we set $\iota = 0$, $T_{EH} = (1 - \tau)\, T_{tot}$ and $B = I_H$ in (3.1). Then, following the same steps for the derivation of (3.8), average harvested energy in TS-PS method can be obtained as (3.26) as

$$\begin{aligned}
\bar{E}_{TS-PS}(\tau, \rho) \approx\, & \tau T_{tot} F (1 - \rho)\, rhS \left(B + \zeta A/2\right) V_t \\
& \times \left[\frac{2}{3}\psi(2\mu_x) + \frac{1}{6}\psi\left(2\mu_x + \sqrt{3}\,(2\sigma_x)\right) + \frac{1}{6}\psi\left(2\mu_x - \sqrt{3}\,(2\sigma_x)\right)\right] \\
& + (1 - \tau)\, T_{tot} FrhSI_H V_t \\
& \times \left[\frac{2}{3}\varphi(2\mu_x) + \frac{1}{6}\varphi\left(2\mu_x + \sqrt{3}\,(2\sigma_x)\right) + \frac{1}{6}\varphi\left(2\mu_x - \sqrt{3}\,(2\sigma_x)\right)\right]
\end{aligned} \tag{3.26}$$

$\overline{BER}_{TS-PS}$ and $\overline{\eta}_{TS-PS}$ can simply calculated respectively from (3.19) and (3.21) by multiplying $\overline{BER}_{PS}$ and $\overline{\eta}_{PS}$ by τ.

To maximize the harvested energy by proper choices of τ and ρ, we can write the optimization problem as

$$\begin{aligned}
\max_{\tau,\rho} \quad & \bar{E}_{TS-PS}(\tau, \rho) \\
s.t. \quad & C_9 : \overline{BER}_{TS-PS} \leq BER_t \\
& C_{10} : \overline{\eta}_{TS-PS} \geq \eta_{th} \\
& C_{11} : 0 \leq \tau \leq 1 \\
& C_{12} : 0 \leq \rho \leq 1
\end{aligned} \tag{3.27}$$

Following similar discussions in Section 3.3, we can express the constraint C_9 as an upper bound on τ and the constraint C_{10} as a lower bound on τ. Noting the range of τ in the constraint C_{11} (i.e., $0 \leq \tau \leq 1$), we can combine these constraints into a single constraint and express it as $\max(0, \eta_{th}/\overline{\eta}_{PS}) \leq \tau \leq \min\left(BER_t \big/ \overline{BER}_{PS}, 1\right)$. Similarly, we need to obtain bounds on the other optimization parameter ρ. Following discussions in Section 3.4, we can express the constraints C_9 and C_{10} as lower bounds of ρ, i.e., $\rho \geq \rho_3$ and $\rho \geq \rho_4$. Here, ρ_3 is obtained by dividing BER_t in ρ_1 defined in (3.20) by τ. Similarly, ρ_4 is obtained by dividing η_{th} in ρ_2 defined in (3.23) by τ.

Noting the range of ρ in the constraint C_{12} (i.e., $0 \leq \rho \leq 1$), we can combine these constraints into a single constraint and express it as $\max(\rho_3, \rho_4) \leq \rho \leq 1$. Under these new constraints, we can rewrite the optimization problem as

$$\begin{aligned} &\max_{\tau,\rho} \bar{E}_{TS-PS}(\tau,\rho) \\ &s.t. \;\; C_{13}: \max\left(0, \frac{\eta_{th}}{\overline{\eta}_{PS}}\right) \leq \tau \leq \min\left(\frac{BER_t}{\overline{BER}_{PS}}, 1\right) \\ &\qquad C_{14}: \max(\rho_3, \rho_4) \leq \rho \leq 1 \end{aligned} \tag{3.28}$$

From (3.26), it is observed that $\overline{E}_{TS-PS}$ has two terms. The first term (proportional to τ) is associated with the first phase where EH and ID are performed while the second term (proportional to $1-\tau$) is associated with the second phase where only EH mode is active. It can be shown that the second term is dominant. Therefore, to maximize the average harvested energy, we need to choose the minimum value of τ while satisfying the constraint C_{13}. This yields the optimum value of τ as $\tau_{opt} = \eta_{th}/\overline{\eta}_{PS}$ where $\overline{\eta}_{PS}$ is a function of ρ. Replacing τ_{opt} in (3.26), we can express average harvested energy as a function of only ρ. Mathematically speaking, the optimization problem now takes the form of

$$\begin{aligned} &\max_{\rho} \bar{E}_{TS-PS}(\rho) \\ &s.t. \;\; C_{15}: \max(\rho_3, \rho_4) \leq \rho \leq 1 \end{aligned} \tag{3.29}$$

Unfortunately, there is no closed form solution for ρ. However, it can be easily found through numerical techniques. Here we utilize the binary search algorithm [56]. The initial value of ρ is set equal to $(\rho_{\min} + \rho_{\max})/2$ with $\rho_{\min} = \max(\rho_3, \rho_4)$ and $\rho_{\max} = 1$. For each value of ρ under consideration, we find $\bar{E}_{TS-PS}$, $\overline{BER}_{TS-PS}$, and $\overline{\eta}_{TS-PS}$ using (3.26), (3.19) and (3.21), respectively. If η_{th} and BER_t were satisfied, $\rho_{\max}$ is updated by that specific value of ρ. Otherwise, $\rho_{\min}$ is updated with that value and the process continues until the the maximum value of $\bar{E}_{TS-PS}$ is found. As a final remark, it should be emphasized that it is not necessary to run this optimization algorithm in real time. For a given set of channel and system parameters (i.e., water type, link distance, turbulence strength, targeted values of spectral efficiency and BER), optimal values can be computed and stored in a look-up table for use.

CHAPTER IV

NUMERICAL RESULTS

In this section, we present the performance of SLIPT methods under consideration for different water types and investigate the effect of channel and system parameters. Unless otherwise stated, we use the following parameters listed in Table 4.1 in our simulations.

Table 4.1: System and channel parameters.

Parameters	**Values**
Block transmission time (T_{tot})	1 s [9]
Receiver aperture diameter (D_r)	20 cm [31]
Responsivity (r)	0.6 A/W [61]
Fill factor (F)	0.75 [61]
Dark saturation current of PD (I_0)	10^{-9} A [61]
Thermal voltage (V_t)	25 mV [61]
Constellation size (M)	16 [16]
Power spectral density of noise (N_0)	10^{-19} W/Hz [16]
Slope efficiency of LD (S)	1.33 W/A [62]
Minimum input bias current (I_L)	200 mA [62]
Maximum input bias current (I_H)	1200 mA [62]
Wavelength (λ)	450 nm [62]
Kinematic viscosity (ν)	1.0576×10^{-6} m^2s^{-1} [46]
Relative strength of temperature and salinity fluctuations (ω)	-1 [46]
Eddy diffusivity ratio (d_r)	1 [46]
Thermal expansion coefficient (α)	2.56×10^{-4}1/°C [46]
Dissipation of mean-squared temperature (χ_T)	$10^{-7}K^2s^{-3}$ [37]
Dissipation rate of turbulent kinetic (ε)	$10^{-5}m^2s^{-3}$ [37]
Extinction coefficient (c)	0.56 [31] (Pure sea) 0.150 [31] (Clear ocean) 0.305 [31] (Coastal water)

In Fig. 4.1, we present harvested energy - spectral efficiency (HE-SE) regions for ADS, TS, PS, and TS-PS methods without optimization, i.e., the switching/splitting factors are set to $\tau = \rho = 0.5$. As a benchmark, we also include the upper bound on the HE-SE region whose derivation can be found in the Appendix C. We consider clear ocean, assume a BER target of $BER_t = 10^{-6}$ and a link distance of $d = 10$ m. Average harvested energies for ADS, TS, PS, and TS-PS methods are plotted based on the derived expressions respectively in (3.8), (3.11), (3.17) and (3.26). As benchmarks, we also include the *exact* expressions calculated through numerical integration, see dashed plots. It can be readily confirmed that our derived expressions and exact expressions match perfectly, i.e., the difference between two curves is very small and can not be observed since it remains within the thickness of line. It is also observed from Fig. 4.1 that the ADS method achieves the largest HE-SE region when no optimization is considered. ADS is then followed by PS, TS-PS and TS methods, respectively.

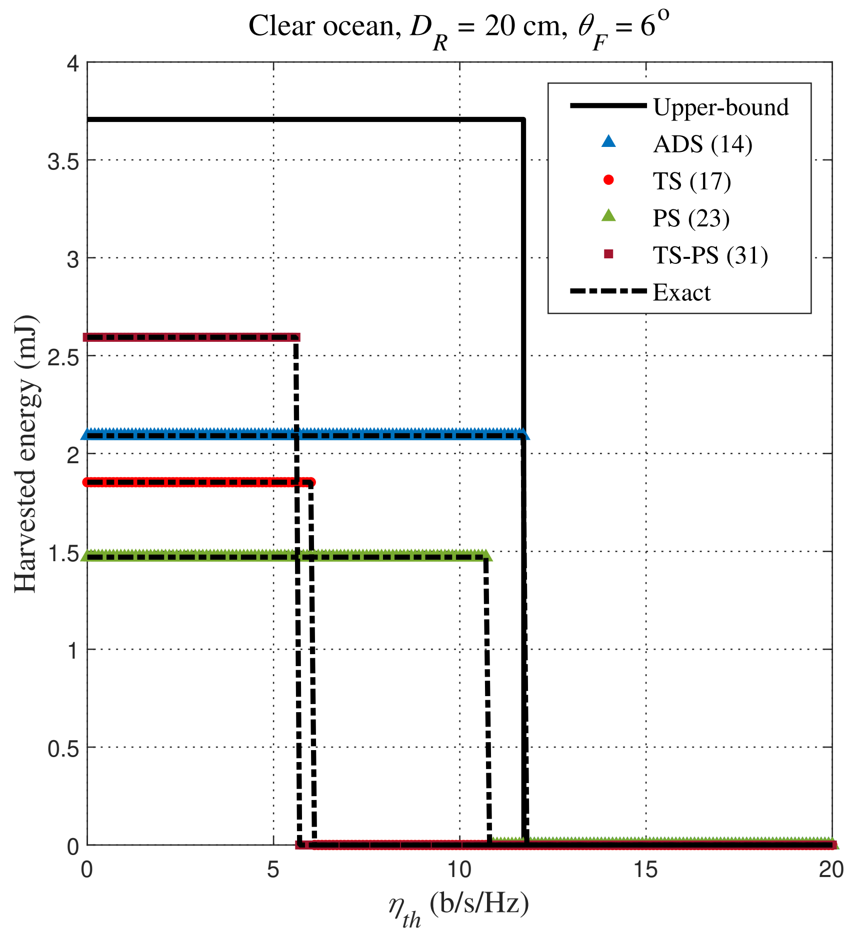

Figure 4.1: Comparison of SLIPT methods without optimization (τ=ρ= 0.5)

In the following, we investigate how much improvement is obtained through optimization of SLIPT methods under consideration. The optimum values of τ and ρ are provided in Table 4.2 for selected values of η_{th}. For example, in TS method, the optimum time switching factor for $\eta_{th} = 1$ b/s/Hz is $\tau_{opt} = 7.41\%$. Recalling that the total block transmission time is selected as $T_{tot} = 1$ s in our simulations, this indicates that only a duration of $T_{ID} = 0.0741$ s is dedicated for ID mode while EH mode has a duration of $T_{EH} = 0.926$ s. For $\eta_{th} = 5$ b/s/Hz and $\eta_{th} = 10$ b/s/Hz, dedicated times for ID mode increase to $T_{ID} = 0.4055$ s and 0.8453 s respectively. In PS method, the optimum power splitting factors for $\eta_{th} = 1$ and 5 b/s/Hz are respectively $\rho_{opt} = 0.71\%$ and 1.59% indicating that almost all power is allocated for

Table 4.2: Optimized values of switching/splitting factors for different values of η_{th}.

Method \ η_{th}	1 b/s/Hz	5 b/s/Hz	10 b/s/Hz
TS (τ_{opt})	7.41%	40.55%	84.53%
PS (ρ_{opt})	0.71%	1.59%	28.12%
TS-PS (τ_{opt}, ρ_{opt})	11.45%, 3.69%	64.31%, 4.25%	100%, 28.12%

EH mode. Even for $\eta_{th} = 10$ b/s/Hz, only 28.12% of the power is spent for ID mode. In TS-PS mode, for $\eta_{th} = 1$ b/s/Hz, 11.45% of the total transmission time and 3.69% of the total power are used for ID mode. As η_{th} increases, the power splitting factor increases slightly while increase in time switching factor is much faster. For $\eta_{th} = 10$ b/s/Hz, it is interesting to note that the whole time is dedicated for ID mode.

In Fig. 4.2, we present HE-SE regions for TS, PS, and TS-PS methods with optimized splitting/switching factors along with ADS. It is observed that optimized TS-PS method achieves the largest HE-SE region. It is then followed by PS, ADS and TS, respectively. It should be further noted that the harvested energy remains constant in ADS method for different η_{th} values. Because the same value of DC bias (B) is used for energy harvesting regardless of the value of spectral efficiency. On the other hand, in optimized TS, PS, and TS-PS methods, as the threshold spectral efficiency increases, the larger portions of splitting and/or switching factor are assigned for information decoding. Therefore, for these methods, the amount of harvested energy decreases as the spectral efficiency increases.

In the rest, we only consider optimized TS-PS method (which provides the best performance among TS and PS variants under consideration) and investigate the effect of water type and system parameters. The performance of ADS method is further included as a benchmark. In the following figures, we use solid lines for optimized TS-PS method and dashed lines for ADS method while different colors specify the relevant parameters.

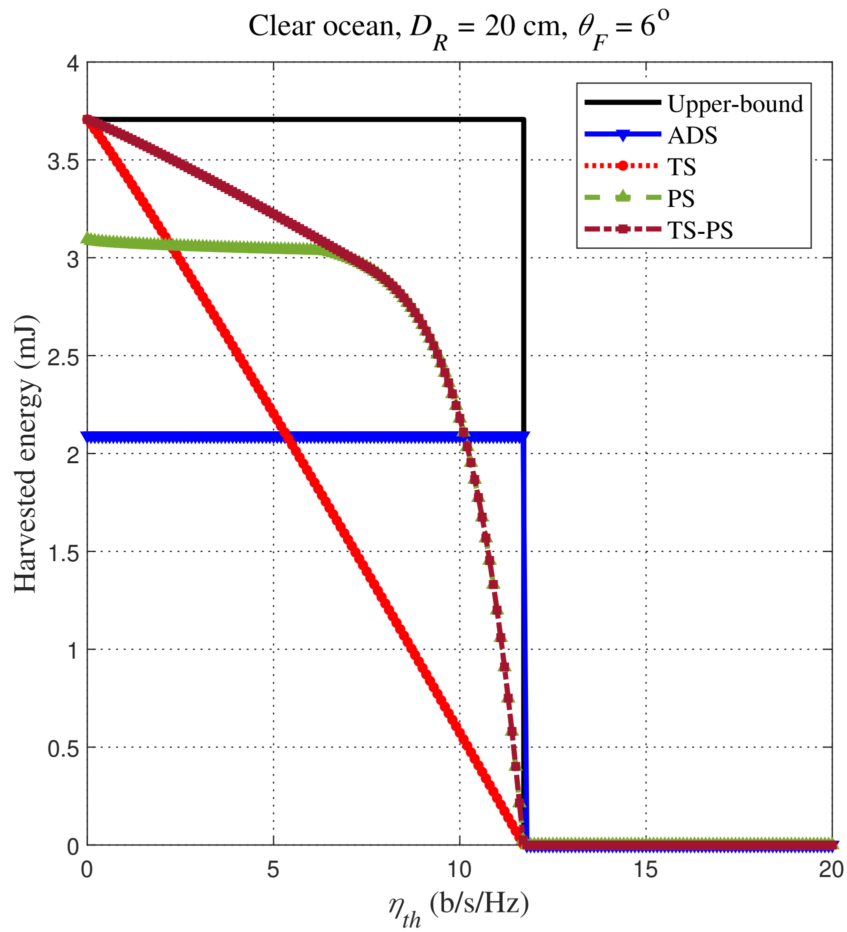

Figure 4.2: Comparison of SLIPT methods with optimization.

In Fig. 4.3, we investigate the effect of water type on the amount of harvested energy with respect to spectral efficiency (η_{th}). It can be observed that more harvested energy is obtained in pure sea (classified as non-turbid water) in comparison to clear ocean and coastal water (classified as turbid water). Turbid water results in large values of extinction coefficient. Thus, the received signal experiences a larger attenuation and eventually results in less amount of harvested energy in comparison to non-turbid water. It can be checked readily from Fig. 4.3 that optimized TS-PS method achieves the largest HE-SE region in comparison with ADS method in all water types and outperforms ADS method for a wide range of spectral efficiency values. For example, ADS method becomes superior only after the spectral efficiency values

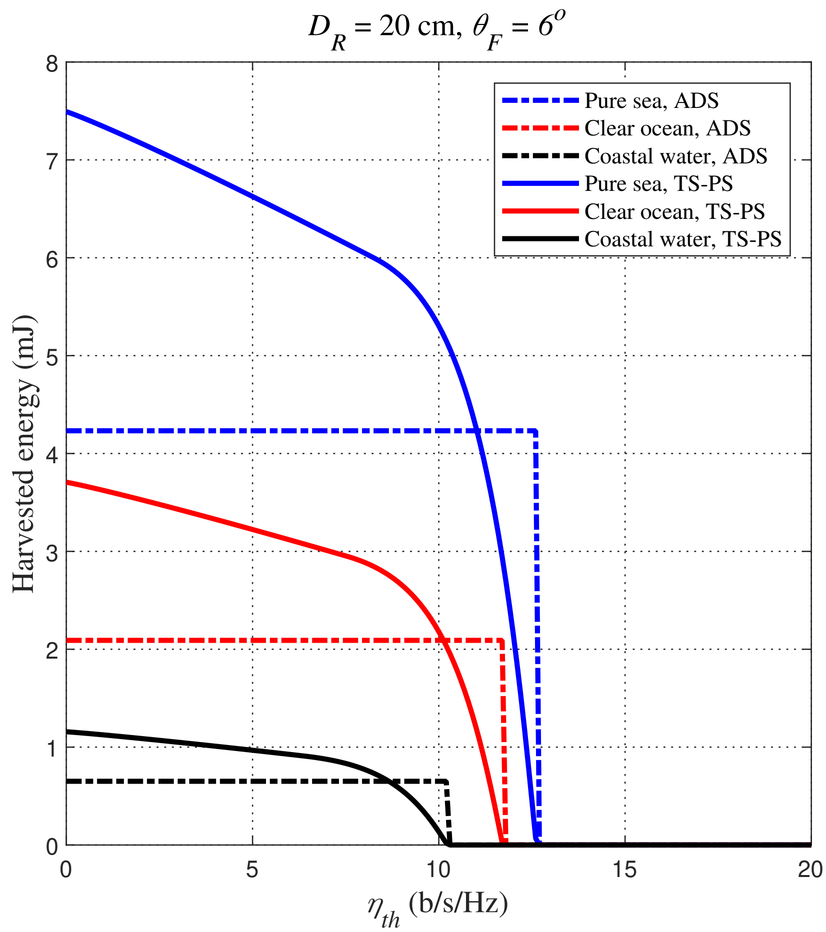

Figure 4.3: Effect of water type on harvested energy.

exceeds $\eta_{th} \cong 9$ b/s/Hz in coastal water. As the turbidity decreases, this threshold value further increases. Specifically, the superiority of ADS method is observed for clear ocean and pure sea only for $\eta_{th} > 10$ b/s/Hz and $\eta_{th} > 11$ b/s/Hz.

In Fig. 4.4, we present the harvested energy with respect to spectral efficiency (η_{th}) and investigate the effect of turbulence strength in clear ocean. We consider three cases, namely 1) $\chi_T = 10^{-7}\,\mathrm{K^2s^{-1}}$, and $\varepsilon = 10^{-5}\,\mathrm{m^2s^{-3}}$, 2) $\chi_T = 5 \times 10^{-7}\,\mathrm{K^2s^{-1}}$, and $\varepsilon = 5 \times 10^{-6}\,\mathrm{m^2s^{-3}}$ and 3) $\chi_T = 10^{-6}\,\mathrm{K^2s^{-1}}$, and $\varepsilon = 10^{-6}\,\mathrm{m^2s^{-3}}$ [37] which yield respectively scintillation indices of $\sigma_I^2 = 0.079$, $\sigma_I^2 = 0.31$, and $\sigma_I^2 = 0.57$. It can be observed that when the scintillation index is sufficiently small, turbulence does not have a significant effect on the amount of harvested energy. For example, the

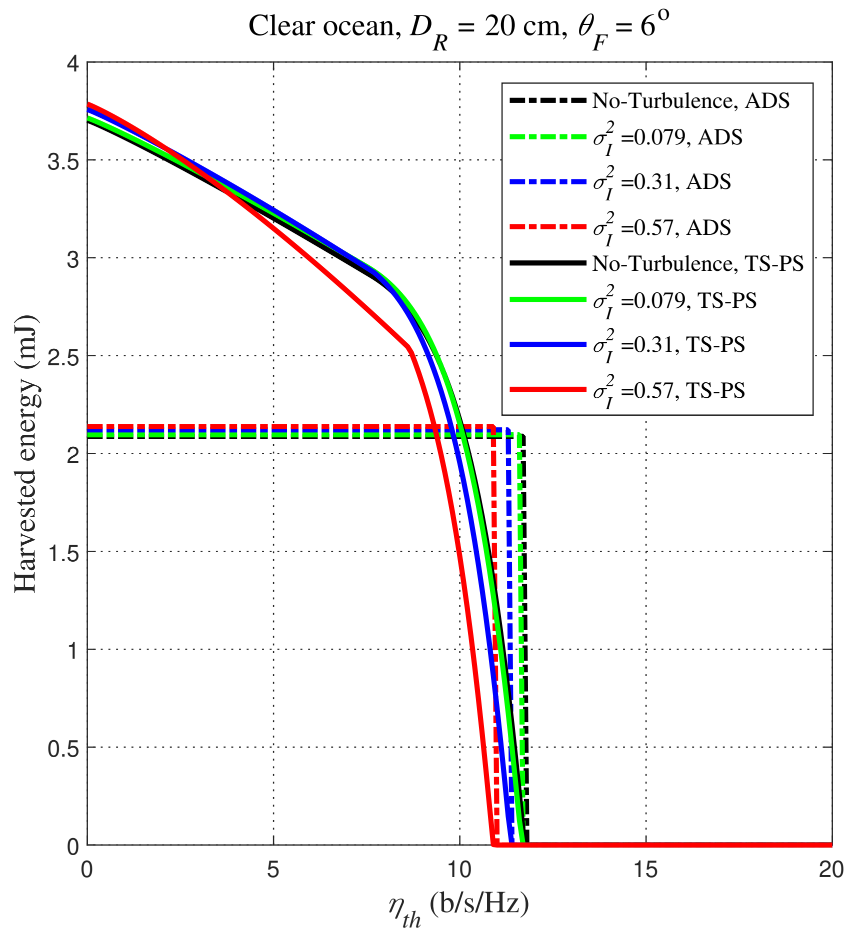

Figure 4.4: Effect of turbulence strength on harvested energy.

curve associated with case 1 coincides with no-turbulence case. As the scintillation index increases, the effect of turbulence strength becomes more pronounced. It can be further noted that optimized TS-PS method achieves the largest HE-SE region in comparison with ADS method for all turbulence strengths and outperforms ADS method for a wide range of spectral efficiency values. The exceptions are the small regions after $\eta_{th} = 10.1$ b/s/Hz for $\sigma_I^2 = 0.079$, $\eta_{th} = 9.8$ b/s/Hz for $\sigma_I^2 = 0.31$ and $\eta_{th} = 9.3$ b/s/Hz for $\sigma_I^2 = 0.57$, where ADS method becomes superior.

In Fig.4.5 and Fig.4.6, we investigate the effect of beam divergence angle on the average harvested energy with respect to the link distance in clear ocean. We consider both $\eta_{th} = 3$ b/s/Hz (Fig.4.5) and $\eta_{th} = 5$ b/s/Hz (Fig.4.6). As expected, when link distance decreases, the receiver can collect more energy and the harvested energy increases. It is also observed that as beam divergence angle decreases, the harvested energy increases since the collimated beam helps the receiver to collect more energy. It can be readily checked from Fig.4.5 that the optimized TS-PS method outperforms ADS method for the whole transmission range and all values of beam divergence angles under consideration when 3 b/s/Hz is considered. For $\eta_{th} = 5$ b/s/Hz, it is observed from Fig.4.6 that optimized TS-PS method outperforms ADS for most cases. Specifically, for $\theta_F = 6^o$, TS-PS method outperforms ADS for the whole transmission range under consideration. For $\theta_F = 12^o$, the situation is similar, but now the performance of two methods coincide for sufficiently large distance (see $d =$ 20 m). For $\theta_F = 18^o$, TS-PS method outperforms ADS for up to $d = 16$ m. After that, it is outperformed by ADS.

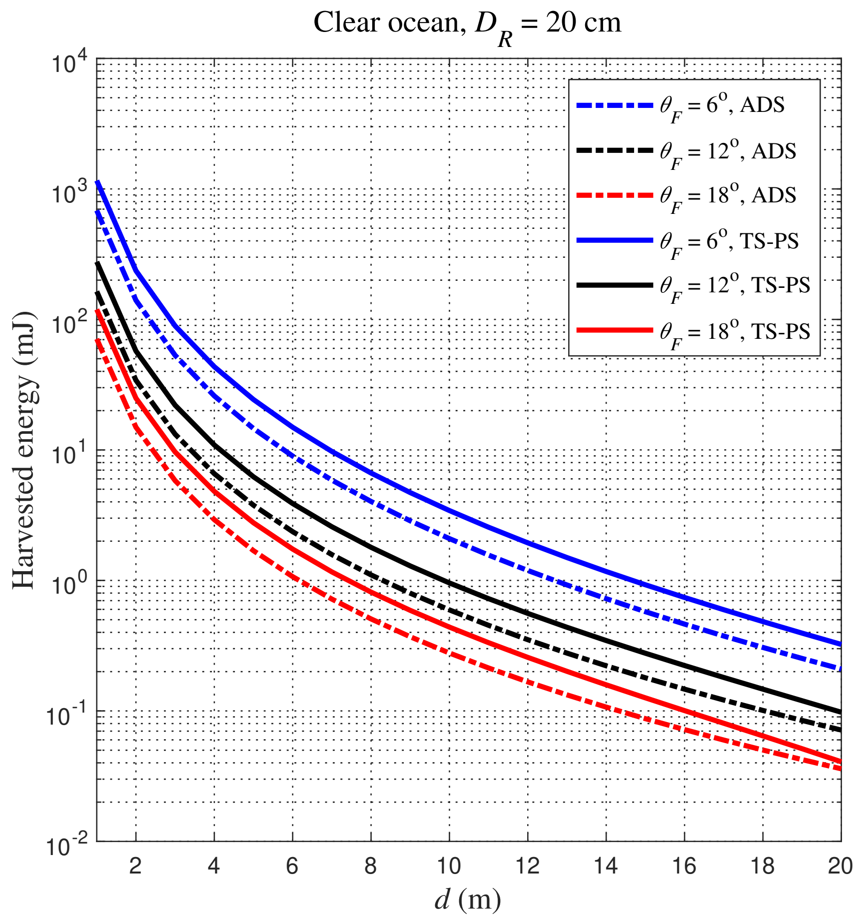

Figure 4.5: Effect of beam divergence angle on harvested energy for $\eta_{th} = 3$ b/s/Hz .

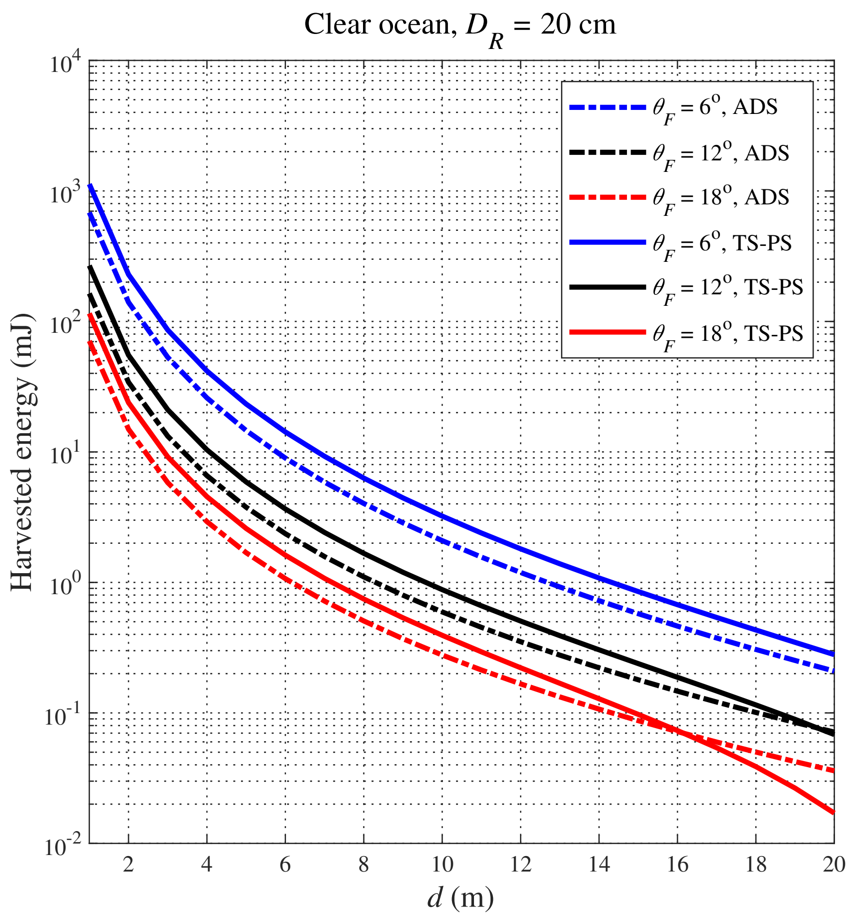

Figure 4.6: Effect of beam divergence angle on harvested energy for $\eta_{th} = 5$ b/s/Hz.

In Figs. 4.7 and 4.8, we investigate the effect of receiver aperture diameter on the average harvested energy with respect to link distance. We consider clear ocean and threshold spectral efficiency values of $\eta_{th} = 3$ b/s/Hz and $\eta_{th} = 5$ b/s/Hz. It is observed that as beam aperture diameter increases, the harvested energy increases since the larger receiver aperture diameter collects more energy. Similar to previous cases, the proposed TS-PS method outperforms ADS method in majority of the cases. Specifically, for $\eta_{th} = 3$ b/s/Hz (see Fig. 4.7), the optimized TS-PS method outperforms ADS method for all receiver aperture diameters under consideration except $D_R = 5$ cm. For $D_R = 5$ cm, the optimized TS-PS and ADS method converge at $d = 16$ m and after this transmission distance the communication is terminated for both methods since the threshold spectral efficiency cannot be satisfied due to the low amount of received power for this small aperture size. For $\eta_{th} = 5$ b/s/Hz (see Fig. 4.8), TS-PS method outperforms ADS for $D_R = 30$ cm, $D_R = 40$ cm and $D_R = 50$ cm. For $D_R = 10$ cm, TS-PS method outperforms ADS for up to 18 m, then the situation reverses after $d = 18$ m. Similarly, for $D_R = 5$ cm, TS-PS method outperforms ADS for up to 12 m while the situation reverses after $d = 12$ m. It can also be seen that, after the distance of $d = 15$ m for $D_R = 5$ cm, the communication is terminated since the threshold spectral efficiency cannot be satisfied due to the low amount of received power.

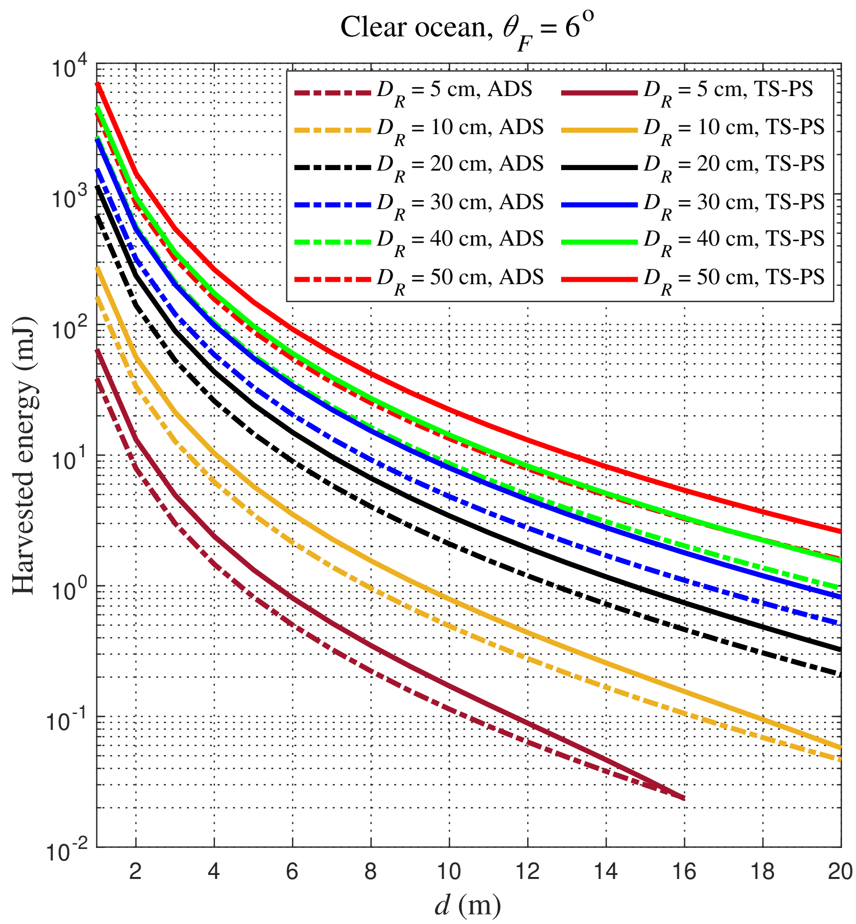

Figure 4.7: Effect of receiver aperture diameter on harvested energy for $\eta_{th} = 3$ b/s/Hz.

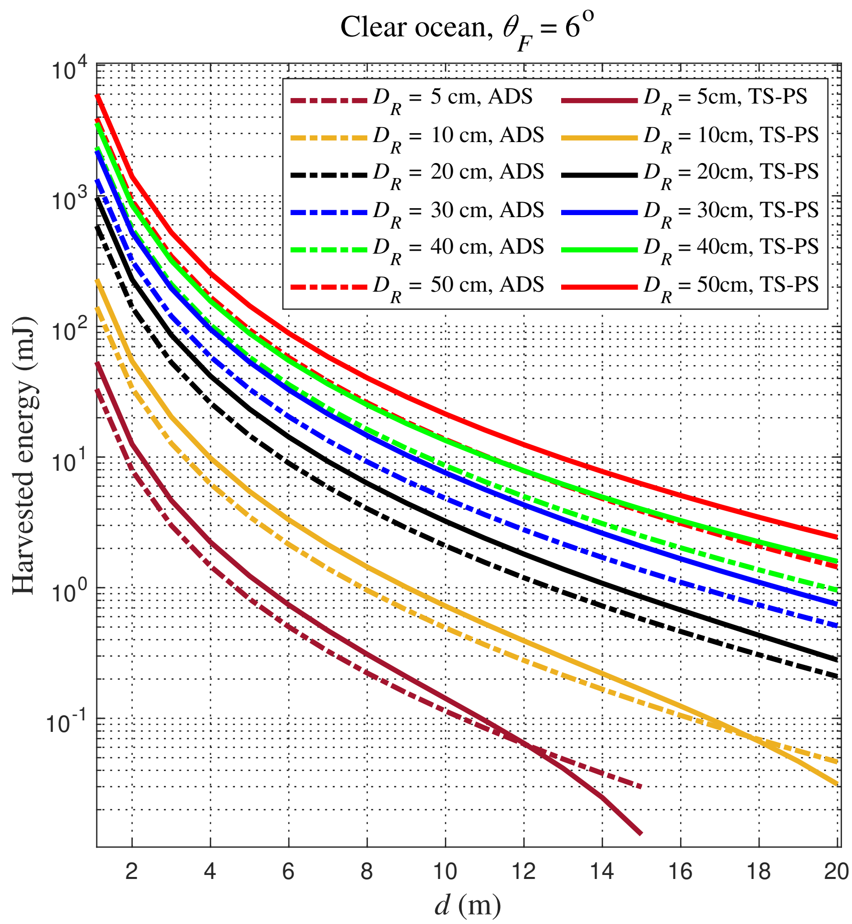

Figure 4.8: Effect of receiver aperture diameter on harvested energy for $\eta_{th} = 5$ b/s/Hz.

As a final remark to demonstrate the practicality of SLIPT for underwater environments, we calculate the lifetime improvement of a sensor node [57], [58]. The sensor node has an operating voltage of 3.6 V and draws a current of 0.15 mA in wake-up mode with duration of 0.3 s and 60 nA in sleep mode with duration of 0.7 s. The power consumption of this sensor node for 1 s is therefore given by $[(0.15\,\mathrm{mA} \times 0.3\ \mathrm{s}) + (60 \times 10^{-6}\,\mathrm{mA} \times 0.7\ \mathrm{s})] \times 3.6\,\mathrm{V} = 0.162$ mW. We assume that the node is powered by a rechargeable lithium-ion battery with capacity of $C = 35$ mAh and nominal voltage of $V = 3.7$ V [59]. The total energy of this battery can be calculated as $E_{battery} = C \times V \times 3600 = 35 \times 3.7 \times 3600 \cong 466$ J. It can be readily calculated that the aforementioned battery can supply this sensor for 35 mAh $\times$ 3.7 V / (0.162 mW $\times$ 24 h/day) = 33 days.

In the following, we calculate how much improvement in lifetime of this sensor node can be obtained through SLIPT. We assume that the UVLC transmitter works in sleep/wake-up mode and has a duty-cycle of 20 s [60]. The transmitter is only active for a duration of $T_{tot} = 1$ s (i.e., wake-up period) in each duty cycle and remains in sleeping mode for the rest. Assume a link distance of $d = 10$ m and threshold spectral efficiency of $\eta_{th} = 5$ b/s/Hz. It can be checked from Fig. 4.2 that the amount of harvested energy in optimized TS-PS method for 1 s is equal to 3.22 mW. Therefore, it takes 466000/3.22 $\cong$ 144720 s to recharge the battery in this method. Considering the duty cycle of transmitter, it will take (20 $\times$ 144720)/ (3600 s/h $\times$ 24 h/day) $\cong$ 33 days to recharge the battery. Recalling that the battery life for this sensor is 33 days, this indicates a 100% lifetime improvement. Following similar steps, it can be found out that the battery can be recharged in 29 days for $\eta_{th} = 1$ b/s/Hz which indicates an improvement of 110% improvement. Lifetime improvements for other SLIPT methods are further provided in Table 4.3. It can be checked that lifetime improvements range between 63% - 110% , 63% - 100% and 15% - 66% respectively for $\eta_{th} = 1$ b/s/Hz , $\eta_{th} = 5$ b/s/Hz, and $\eta_{th} = 10$ b/s/Hz.

Table 4.3: Required recharging time in clear ocean ($d = 10$ m).

Methods		ADS	Optimized TS	Optimized PS	Optimized TS-PS
$\eta_{th} = 1$ b/s/Hz	Harvested energy (mJ)	2.09 mJ	3.43 mJ	3.05 mJ	3.62 mJ
	Recharging time (days)	$\sim$ 52 days	$\sim$ 32	$\sim$ 35 days	$\sim$ 30 days
	Lifetime improvement (percentage)	$\sim$ 63%	$\sim$ 103%	$\sim$ 94%	$\sim$ 110%
$\eta_{th} = 5$ b/s/Hz	Harvested energy (mJ)	2.09 mJ	2.20 mJ	3.02 mJ	3.22 mJ
	Recharging time (days)	$\sim$ 52 days	$\sim$ 49 days	$\sim$ 35 days	$\sim$ 33 days
	Lifetime improvement (percentage)	$\sim$ 63%	$\sim$ 67%	$\sim$ 94%	$\sim$ 100%
$\eta_{th} = 10$ b/s/Hz	Harvested energy (mJ)	2.09 mJ	0.57 mJ	2.16 mJ	2.18 mJ
	Recharging time (days)	$\sim$ 52 days	$\sim$ 189 days	$\sim$ 50 days	$\sim$ 50 days
	Lifetime improvement (percentage)	$\sim$ 63%	$\sim$ 15%	$\sim$ 66%	$\sim$ 66%

CHAPTER V

CONCLUSION

In this thesis, we investigated the performance of UVLC systems with SLIPT capability. We investigated different SLIPT methods based on time switching and/or power splitting to balance the trade-off between the harvested energy and spectral efficiency under a targeted BER constraint.

In chapter 2, we first presented the signal models and SLIPT methods under consideration. Then, we describe the path loss and turbulence-induced fading models to characterize the underwater propagation environment.

In chapter 3, first, we derived closed-form expressions for the average harvested energy, BER and spectral efficiency over LN turbulence channels. Then we solved optimization problems for each method and found the optimum values of time switching and power splitting factors to maximize the amount of harvested energy while satisfying the constraints on BER and spectral efficiency.

In chapter 4, we present the performance of SLIPT methods under considerationfor different water types and investigate the effect of channel and system parameters. Our numerical results revealed that optimization of switching/splitting factors significantly extend the HE-SE regions of SLIPT methods under consideration. In particular, the proposed TS, PS and TS-PS methods outperform ADS method especially for low and medium values of spectral efficiency. As the threshold spectral efficiency increases, the improvements of proposed methods over the ADS decrease to a certain extent, but are still significant in most cases. We also provided extensive numerical results to examine the effects of water types, turbulence strength and system parameters (i.e., beam divergence angle, and aperture diameter) on the average harvested energy. Our results further demonstrated that the harvested energy is sufficient to recharge a lithium-ion battery module within a reasonable amount of time under typical settings and can significantly extend the lifetime of an underwater sensor node.

Appendix A

In this appendix, we present the underwater spatial power spectrum model required for the calculation of scintillation index in (2.8).

The spatial power spectrum as a function of the magnitude of the spatial frequency (κ) is given by [46]

$$\Phi(\kappa) = \frac{1}{4\pi\kappa^2} C_0 \chi_n \varepsilon^{-1/3} \kappa^{-5/3} \left(1 + C_1 (\kappa\xi)^{2/3}\right) \phi(\kappa, \omega) \tag{5.1}$$

where C_0 and C_1 are constants and respectively, equal to 0.72 and 2.35. Here, ε is the dissipation rate of turbulent kinetic energy per unit mass of fluid and ξ is Kolmogorov microscale length. Let υ denote the kinematic viscosity. The Kolmogorov microscale length is then given by $\xi = (\upsilon^3/\varepsilon)^{1/4}$.

In (5.1), χ_n is the dissipation rate of mean-squared refractive index and defined as $\chi_n = \alpha^2 \chi_T + \beta^2 \chi_S + 2\alpha\beta\chi_T\chi_S$ where α is the thermal expansion coefficient and β is the saline (i.e., Haline) contraction coefficient.χ_T, χ_S and χ_{TS} are, respectively, the dissipation rate of mean-squared temperature, the dissipation rate of mean-squared salinity and the correlation of χ_T and χ_S. They are given as

$$\chi_T = K_T \left(\frac{dT_0}{dz}\right)^2 \tag{5.2}$$

$$\chi_S = K_S \left(\frac{dS_0}{dz}\right)^2 \tag{5.3}$$

$$\chi_{TS} = \frac{K_T + K_S}{2} \left(\frac{dT_0}{dz}\right) \left(\frac{dS_0}{dz}\right) \tag{5.4}$$

where K_S and K_T denote eddy diffusivity of salinity and temperature, respectively. Here, dT_0/dz and dS_0/dz denote the temperature and salinity difference between top and bottom boundaries, respectively.

In (5.1), $\phi(\kappa,\omega)$ is given by

$$\begin{aligned}\phi(\kappa,\omega) = &\omega^2 \exp\left(-C_0 C_1^{-2} P_T^{-1}\delta\right) + d_r \exp\left(-C_0 C_1^{-2} P_S^{-1}\delta\right) \\ &+ \omega(d_r+1)\exp\left(-C_0 C_1^{-2}(2P_{TS})^{-1}\delta\right)\end{aligned} \tag{5.5}$$

where $\delta = 1.5C_1^2(\kappa\eta)^{4/3} + C_1^3(\kappa\eta)^2$ and $\omega = \alpha(dT_0/dz)/\beta(dS_0/dz)$ is the relative strength of temperature and salinity fluctuations. Here, $P_T = \nu D_T^{-1}$ and $P_S = \upsilon D_S^{-1}$ are respectively the Prandtl number for temperature and salinity, and P_{TS} is the one-half of the harmonic mean of P_T and P_S. D_T and D_S denote molecular diffusivity of temperature and salinity, respectively.

Appendix B

A common approximation on the probability of symbol error is given by [50]

$$SER \approx \overline{N} Q\left(\sqrt{\frac{\left(d_{\min}/2\right)^2}{N_0}}\right) \tag{5.6}$$

where $d_{\min} = 2P\sqrt{T_s}\Big/(M-1)$ is the minimum Euclidean distance of the signal constellation [50] and $P = rIhSE[x]$ [12], [16] is the average optical received power. Here, $\overline{N} = 2\,(M-1)/M$ is the average number of constellation points which are located $d_{\min}$ away from any point. Therefore, (5.6) can be written as

$$SER \approx \frac{2\,(M-1)}{M} Q\left(\sqrt{\frac{\left(rIhSE\,[x]\right)^2 T_s}{\left(M-1\right)^2 N_0}}\right) \tag{5.7}$$

Under the assumption of Gray coding and substituting $N_0 = 2T_s\sigma^2$, the BER (conditioned on I) of M-PAM signal can be approximated as [16], [50], [51]

$$\begin{aligned} BER_{tot} &\approx \frac{SER}{\log_2 M} \\ &= \frac{2\,(M-1)}{M\log_2 M} Q\left(\sqrt{\frac{\gamma}{2(M-1)^2}}\right) \end{aligned} \tag{5.8}$$

where γ is defined as

$$\gamma = \frac{\left(rIhSE\,[x]\right)^2}{\sigma^2} \tag{5.9}$$

The BER expression in (5.8), (denoted by BER_{tot}) builds upon the assumption that the whole transmission frame (with a duration of T_{tot} spanning N symbols) is used for ID. However, in our case, $(1-\tau)\,N$ symbols (with a duration of T_{EH}) are used for EH mode while τN symbols (with a duration of T_{ID}) are used for ID model. Therefore, BER needs to be properly scaled as

$$BER = \frac{T_{ID}}{T_{tot}} BER_{tot} \tag{5.10}$$

Replacing (5.8) in (5.10), we obtain

$$BER \approx \frac{T_{ID}}{T_{tot}} \frac{2\left(M-1\right)}{M \log_2 M} Q\left(\sqrt{\frac{\gamma}{2{(M-1)}^2}}\right) \tag{5.11}$$

which is the BER expression in (3.2).

Appendix C

An upper bound on the HE-SE region can be defined as [12]

$$S = \{(E, \eta) : E \leq E_{\max}, \eta \leq \eta_{\max}\} \tag{5.12}$$

which is a rectangular region specified by the origin and the three vertices $(0, E_{\max})$, $(\eta_{\max}, 0)$, and $(\eta_{\max}, E_{\max})$.

$E_{\max}$ is the maximum achievable harvested energy which can be obtained by assigning the whole transmission block and received power to EH mode (i.e., $\tau = 0$, $\rho = 0$). Therefore, we have $I_{AC} = 0$ and $I_{DC} = I'_{DC}$. Setting the DC bias at its maximum value (i.e., $B = I_H$), we obtain $I'_{DC} = rIhSI_H$. Replacing T_{EH} and I'_{DC} within (3.1), we obtain the maximum achievable harvested energy (conditioned on I) as

$$E_{\max} = T_{tot} F r I h S I_H V_t \ln\left(1 + \frac{rIhSI_H}{I_0}\right) \tag{5.13}$$

Taking an expectation with respect to I and following similar steps which lead to (3.8) based on the Holtzmann approximation, we obtain

$$\bar{E}_{max} \approx T_{tot} F r h S I_H V_t \left[\frac{2}{3}\nu\left(2\mu_x\right) + \frac{1}{6}\nu\left(2\mu_x + \sqrt{3}\left(2\sigma_x\right)\right) + \frac{1}{6}\nu\left(2\mu_x - \sqrt{3}\left(2\sigma_x\right)\right)\right] \tag{5.14}$$

where $\nu(z) = \exp(z)\ln(1 + r\exp(z)\, hSI_H/I_0)$.

$\eta_{\max}$ is the maximum achievable spectral efficiency which can be obtained by assigning the whole transmission block and received power to ID mode (i.e., $\tau = 1$, $\rho = 1$). Setting the maximum value for the peak amplitude of signal, i.e., $A = (I_H - I_L)/2$ in (3.3), we obtain the maximum value of SNR. Replacing $T_{ID} = T_{tot}$ and maximum SNR within (3.4), we obtain

$$\eta_{\max} = \frac{1}{2}\log_2\left(1 + \frac{e(rIhSA)^2}{2\pi\sigma^2}\right) \tag{5.15}$$

Taking an expectation of (5.15) with respect to I and following Holtzmann approximation similar to above, we obtain

$$\begin{aligned}\overline{\eta}_{\max} \approx \frac{1}{2}\Bigg[&\frac{2}{3}\log_2\left(1+\frac{e(rhSe^{2\mu_x}(I_H - I_L))^2}{8\pi\sigma^2}\right)\\ &+\frac{1}{6}\log_2\left(1+\frac{e\left(rhSe^{2\mu_x+2\sqrt{3}\sigma_x}(I_H - I_L)\right)^2}{8\pi\sigma^2}\right)\\ &+\frac{1}{6}\log_2\left(1+\frac{e\left(rhSe^{2\mu_x-2\sqrt{3}\sigma_x}(I_H - I_L)\right)^2}{8\pi\sigma^2}\right)\Bigg]\end{aligned} \tag{5.16}$$

Bibliography

[1] C. M. Gussen, P. S. Diniz, M. L. Campos, W. A. Martins, F. M. Costa, and J. N. Gois, "A survey of underwater wireless communication technologies," *J. Commun. Inf. Sys.*, vol. 31, no. 1, pp. 242–255, 2016.

[2] G. Han, X. Long, C. Zhu, M. Guizani, and W. Zhang, "A high-availability data collection scheme based on multi-AUVs for underwater sensor networks," *IEEE Trans. Mobile Comput.*, vol. 19, no. 5, pp. 1010–1022, 2020.

[3] J. I. d. O. Filho, A. Trichili, B. S. Ooi, M. Alouini, and K. N. Salama, "Toward Self-Powered Internet of Underwater Things Devices," *IEEE Commun. Mag.*, vol. 58, no. 1, pp. 68–73, 2020.

[4] S. Sendra, J. Lloret, J. M. Jimenez, and L. Parra, "Underwater acoustic modems," *IEEE Sensors J.*, vol. 16, no. 11, pp. 4063–4071, 2016.

[5] Z. Zeng, S. Fu, H. Zhang, Y. Dong, and J. Cheng, "A survey of underwater optical wireless communications," *IEEE Commun. Surveys Tuts.*, vol. 19, no. 1, pp. 204–238, 2017.

[6] H. Kaushal and G. Kaddoum, "Underwater Optical Wireless Communication," *IEEE Access*, vol. 4, pp. 1518–1547, 2016.

[7] N. Saeed, A. Celik, T. Y. Al-Naffouri, and M.-S. Alouini, "Energy harvesting hybrid acoustic-optical underwater wireless sensor networks localization," *Sensors*, vol. 18, no. 1, p. 51, 2018.

[8] B. S. Srujana, P. Mathews, and V. Harigovindan, "Multi-source energy harvesting system for underwater wireless sensor networks," *Procedia Comput. Sci.*, vol. 46, pp. 1041–1048, 2015.

[9] P. D. Diamantoulakis, G. K. Karagiannidis, and Z. Ding, "Simultaneous lightwave information and power transfer (SLIPT)," *IEEE Trans. on Green Commun. Netw.*, vol. 2, no. 3, pp. 764–773, 2018.

[10] T. Rakia, H. Yang, F. Gebali, and M. Alouini, "Optimal design of dual-hop VLC/RF communication system with energy harvesting," *IEEE Commun. Lett.*, vol. 20, no. 10, pp. 1979–1982, 2016.

[11] X. Lu, P. Wang, D. Niyato, D. I. Kim, and Z. Han, "Wireless networks with RF energy harvesting: A contemporary survey," *IEEE Commun. Surveys Tuts.*, vol. 17, no. 2, pp. 757–789, 2015.

[12] X. Zhou, R. Zhang, and C. K. Ho, "Wireless information and power transfer: Architecture design and rate-energy tradeoff," *IEEE Trans. Commun.*, vol. 61, no. 11, pp. 4754–4767, 2013.

[13] I. Krikidis, S. Timotheou, S. Nikolaou, G. Zheng, D. W. K. Ng, and R. Schober, "Simultaneous wireless information and power transfer in modern communication systems," *IEEE Commun. Mag.*, vol. 52, no. 11, pp. 104–110, 2014.

[14] A. El Shafie, K. Tourki, and N. Al-Dhahir, "An artificial-noise-aided hybrid TS/PS scheme for OFDM-based SWIPT systems," *IEEE Commun. Lett.*, vol. 21, no. 3, pp. 632–635, 2017.

[15] K. Xu, Z. Shen, Y. Wang, X. Xia, and D. Zhang, "Hybrid time-switching and power splitting SWIPT for full-duplex massive MIMO systems: A beam-domain approach," *IEEE Trans. Vehic. Technol.*, vol. 67, no. 8, pp. 7257–7274, 2018.

[16] H. G. Sandalidis, A. Vavoulas, T. A. Tsiftsis, and N. Vaiopoulos, "Illumination, data transmission, and energy harvesting: The threefold advantage of VLC," *Appl. opt.*, vol. 56, no. 12, pp. 3421–3427, 2017.

[17] J. Wang, S. Lin, Y. Qiu, N. Huang, and J. Wang, "Tradeoff between secrecy capacity and harvested energy for secure visible light communications with SWIPT," *IEEE Access*, vol. 7, pp. 29543–29552, 2019.

[18] S.-M. Kim and J.-S. Won, "Simultaneous reception of visible light communication and optical energy using a solar cell receiver," in *Proc. IEEE Int. Conf. ICT Convergence (ICTC), Jeju Island, South Korea,*, pp. 896–897, 2013.

[19] Z. Wang, D. Tsonev, S. Videv, and H. Haas, "Towards self-powered solar panel receiver for optical wireless communication," in *Proc. IEEE Int. Conf. Commun. (ICC), Sydney, NSW, Australia*, pp. 3348–3353, 2014.

[20] Z. Wang, D. Tsonev, S. Videv, and H. Haas, "On the design of a solar-panel receiver for optical wireless communications with simultaneous energy harvesting," *IEEE J. Sel. Areas in Commun.*, vol. 33, no. 8, pp. 1612–1623, 2015.

[21] J. Fakidis, S. Videv, H. Helmers, and H. Haas, "0.5-Gb/s OFDM-Based laser data and power transfer using a gaas photovoltaic cell," *IEEE Photon. Technol. Lett.*, vol. 30, no. 9, pp. 841–844, 2018.

[22] J. Fakidis, H. Helmers, and H. Haas, "Simultaneous wireless data and power transfer for a 1-Gb/s gaas vcsel and photovoltaic link," *IEEE Photon. Technol. Lett.*, vol. 32, no. 19, pp. 1277–1280, 2020.

[23] S. Zhang, D. Tsonev, S. Videv, S. Ghosh, G. A. Turnbull, I. D. Samuel, and H. Haas, "Organic solar cells as high-speed data detectors for visible light communication," *Optica*, vol. 2, no. 7, pp. 607–610, 2015.

[24] I. Tavakkolnia, L. K. Jagadamma, R. Bian, P. P. Manousiadis, S. Videv, G. A. Turnbull, I. D. Samuel, and H. Haas, "Organic photovoltaics for simultaneous energy harvesting and high-speed mimo optical wireless communications," *Light: Science & Applications*, vol. 10, no. 1, pp. 1–11, 2021.

[25] J. Jalbert, J. Baker, J. Duchesney, P. Pietryka, W. Dalton, D. Blidberg, S. Chappell, R. Nitzel, and K. Holappa, "A solar-powered autonomous underwater vehicle," in *Proc. MTS/IEEE Oceans Conf., San Diego, CA, USA*, vol. 2, pp. 1132–1140, 2003.

[26] D. M. Crimmins, C. T. Patty, M. A. Beliard, J. Baker, J. C. Jalbert, R. J. Komerska, S. G. Chappell, and D. R. Blidberg, "Long-endurance test results of the solar-powered AUV system," in *Proc. MTS/IEEE Oceans Conf., Boston, MA, USA*, pp. 1–5, 2006.

[27] M. K. Amruta and M. T. Satish, "Solar powered water quality monitoring system using wireless sensor network," in *Proc. IEEE Int. Mutli-Conf. Autom., Comput., Commun., Control Compressed Sens. (iMac4s)*, pp. 281–285, 2013.

[28] M. Arima, T. Okashima, and T. Yamada, "Development of a solar-powered underwater glider," in *Proc. IEEE Symp. Underwater Technol. Workshop Sci. Use of Submar. Cables and Rel. Technol., Kobe, Japan*, pp. 1–5, 2011.

[29] S. Ghasvarianjahromi, M. Karbalayghareh, P. D. Diamantoulakis, G. K. Karagiannidis, and M. Uysal, "Simultaneous lightwave information and power transfer in underwater visible light communications," in *Proc. IEEE 30th Annu. Int. Symp. Personal, Indoor and Mobile Radio Commun. (PIMRC)*, pp. 1–6, 2019.

[30] C. Gabriel, M.-A. Khalighi, S. Bourennane, P. Léon, and V. Rigaud, "Monte-carlo-based channel characterization for underwater optical communication systems," *IEEE/OSA J. Opt. Commun.Netw.*, vol. 5, no. 1, pp. 1–12, 2013.

[31] M. Elamassie, F. Miramirkhani, and M. Uysal, "Performance characterization of underwater visible light communication," *IEEE Trans. Commun.*, vol. 67, no. 1, pp. 543–552, 2019.

[32] A. Goldsmith, *Wireless communications*. Cambridge university press, 2005.

[33] S. Dimitrov, S. Sinanovic, and H. Haas, "Signal shaping and modulation for optical wireless communication," *IEEE/OSA J. Lightw. Technol.*, vol. 30, no. 9, pp. 1319–1328, 2012.

[34] P. T. Krein and R. S. Balog, "Cost-effective hundred-year life for single-phase inverters and rectifiers in solar and led lighting applications based on minimum capacitance requirements and a ripple power port," in *Proc. 24th Annu. IEEE Appl. Power Electron. Conf. Expo.*, pp. 620–625, 2009.

[35] A. C. Kyritsis and N. P. Papanikolaou and E. C. Tatakis, "A novel parallel active filter for current pulsation smoothing on single stage grid-connected AC-PV modules," in *Proc. European Conf. Power Electron. App.*, pp. 1–10, 2007.

[36] C. D. Mobley, B. Gentili, H. R. Gordon, Z. Jin, G. W. Kattawar, A. Morel, P. Reinersman, K. Stamnes, and R. H. Stavn, "Comparison of numerical models

for computing underwater light fields," *Appl. Opt.*, vol. 32, no. 36, pp. 7484–7504, 1993.

[37] O. Korotkova, N. Farwell, , and E. Shchepakina, "Light scintillation in oceanic turbulence," *Waves Random Complex Media*, vol. 22, no. 2, pp. 260–266, 2012.

[38] C. E. Richmond and S. A. Woodin, "Short-term fluctuations in salinity: effects on planktonic invertebrate larvae," *Marine Ecology Progress Series*, vol. 133, pp. 167–177, 1996.

[39] J. A. Simpson, B. L. Hughes, and J. F. Muth, "A spatial diversity system to measure optical fading in an underwater communications channel," in *OCEANS 2009*, pp. 1–6, 2009.

[40] D. Blanchard and A. Woodcock, "Bubble formation and modification in the sea and its meteorological significance," *Tellus*, vol. 9, no. 2, pp. 145–158, 1957.

[41] M. D. Anguelova and P. Huq, "Effects of salinity on bubble cloud characteristics," *Journal of Marine Science and Engineering*, vol. 6, no. 1, p. 1, 2018.

[42] Y. Ata and Y. Baykal, "Scintillations of optical plane and spherical waves in underwater turbulence," *J. Opt. Soc. Am. A*, vol. 31, no. 7, pp. 1552–1556, 2014.

[43] M. V. Jamali, A. Mirani, A. Parsay, B. Abolhassani, P. Nabavi, A. Chizari, P. Khorramshahi, S. Abdollahramezani, and J. A. Salehi, "Statistical Studies of Fading in Underwater Wireless Optical Channels in the Presence of Air Bubble, Temperature, and Salinity Random Variations," *IEEE Trans. Commun.*, vol. 66, no. 10, pp. 4706–4723, 2018.

[44] Z. Vali, A. Gholami, Z. Ghassemlooy, M. Omoomi, , and D. Michelson, "Experimental study of the turbulence effect on underwater optical wireless communications," *Appl. Opt.*, vol. 57, no. 28, p. 8314–8319, 2018.

[45] M. Sait, X. Sun, O. Alkhazragi, N. Alfaraj, M. Kong, T. K. Ng, and B. S. Ooi, "The effect of turbulence on NLOS underwater wireless optical communication channels," *Chin. Opt. Lett.*, vol. 17, no. 10, 2019.

[46] M. Elamassie, M. Uysal, Y. Baykal, M. Abdallah, and K. Qaraqe, "Effect of eddy diffusivity ratio on underwater optical scintillation index," *J. Opt. Soc. Am. A*, vol. 34, no. 11, pp. 1969–1973, 2017.

[47] C. Li, W. Jia, Q. Tao, and M. Sun, "Solar cell phone charger performance in indoor environment," in *Proc. IEEE 37th Annu. Northeast Bioeng. Conf. (NEBEC)*, pp. 1–2, 2011.

[48] F. M. González-Longatt *et al.*, "Model of photovoltaic module in Matlab," *Ii Cibelec*, pp. 1–5, 2005.

[49] T. Esram and P. L. Chapman, "Comparison of photovoltaic array maximum power point tracking techniques," *IEEE Trans. Energy Convers.*, vol. 22, no. 2, pp. 439–449, 2007.

[50] J. R. Barry, *Wireless infrared communications.* Springer Science & Business Media, 1994.

[51] Z. Ghassemlooy, W. Popoola, and S. Rajbhandari, *Optical wireless communications: System and channel modelling with Matlab®.* CRC press, 2019.

[52] T. A. Tsiftsis, H. G. Sandalidis, G. K. Karagiannidis, and M. Uysal, "Optical wireless links with spatial diversity over strong atmospheric turbulence channels," *IEEE Trans. Wireless Commun.*, vol. 8, no. 2, pp. 951–957, 2009.

[53] X. Zhu and J. M. Kahn, "Free-space optical communication through atmospheric turbulence channels," *IEEE Trans. Commun.*, vol. 50, no. 8, pp. 1293–1300, 2002.

[54] J. Wang, Q. Hu, J. Wang, M. Chen, and J. Wang, "Tight bounds on channel capacity for dimmable visible light communications," *J. Lightw. Technol.*, vol. 31, no. 23, pp. 3771–3779, 2013.

[55] J. M. Holtzman, "A simple, accurate method to calculate spread-spectrum multiple-access error probabilities," *IEEE Trans. Commun.*, vol. 40, no. 3, pp. 461–464, 1992.

[56] F. Vahid, D. D. Gajski, and J. Gong, "A binary-constraint search algorithm for minimizing hardware during hardware/software partitioning," in *Proc. EURO-DAC*, vol. 94, pp. 214–219, 1994.

[57] M. E. Sayed, M. P. Nemitz, S. Aracri, A. C. McConnell, R. M. McKenzie, and A. A. Stokes, "The limpet: A ROS-enabled multi-sensing platform for the ORCA hub," *Sensors*, vol. 18, no. 10, p. 3487, 2018.

[58] SILICON LABS, *Digital I^2C Humidity and Temperature Sensor*, 8 2016. Rev. 1.2.

[59] PowerStream, *PowerStream Li-ion Coin Cell*, 7 2005. Rev. 1.

[60] R. W. Coutinho, A. Boukerche, L. F. Vieira, and A. A. Loureiro, "Modeling and analysis of opportunistic routing in low duty-cycle underwater sensor networks," in *Proc. 18th ACM MSWiM, Cancún.*, pp. 125–132, 2015.

[61] E. Lorenzo, *Solar electricity: engineering of photovoltaic systems.* Earthscan/James & James, 1994.

[62] THORLABS, *450 nm Multimode Laser Diode, 1600 mW*, 2 2016. Rev. A.

VITA

Sara Ghasvarianjahromi (Student Member, IEEE) received the B.Sc. degree in electrical and electronics engineering from the Islamic Azad University of Science and Research of Fars, Shiraz, Iran in 2013. She had been an active member of the WINEL Research Lab at Yazd University between 2014-2017. She is currently working toward the M.Sc. degree in communication systems engineering with the Communication Theory and Technologies (CT&T) Research Group at the Ozyegin University, Istanbul, Turkey. Her current research interests include optical wireless communications, wireless power transfer, optimization algorithms, and energy harvesting.